

## Figure captions

**Figure 1.** A comparison of the time series of monthly kernel-estimated changes in total-sky SW fluxes (red) with monthly anomalies of total-sky SW fluxes extracted from **ERA5** (black) at surface (SFC; a-f) and top-of-atmosphere (TOA; g-l) for the six ARM sites: SGP C1, NSA C1, TWP C1, TWP C2, TWP C3, and ENA C1. The kernel-estimated responses are calculated using **ERA5** water vapor and surface albedo.

**Figure 2.** Same as Figure 1, but for monthly kernel-estimated changes in total-sky LW fluxes (red) and monthly anomalies of total-sky LW fluxes extracted from **ERA5** (black). The kernel-estimated responses are calculated using **ERA5** water vapor and air and surface temperature.

**Figure 3.** Scatter plots for monthly anomalies of total-sky SW and LW fluxes from **ERA5** versus monthly kernel-estimated changes in total-sky SW and LW fluxes at SFC and TOA calculated using the **ERA5** state variables for the six ARM sites.

**Figure 4.** Scatter plots for monthly anomalies of observed total-sky SW and LW fluxes from **ARM (SFC) and CERES (TOA)** versus monthly kernel-estimated changes in total-sky SW and LW fluxes calculated using the **ARM** state variables at SFC and TOA for the six ARM sites.

**Figure 5.** Decomposition of monthly kernel-estimated changes in **ARM** total-sky SW fluxes at SFC (a-f) and TOA (m-r) into SW water vapor (red), surface albedo (blue), and cloud (orange) kernel-estimated changes for the six ARM sites. These kernel-estimated responses are calculated using **ARM-observed** water vapor and surface albedo. Black line represents monthly anomalies of observed total-sky SW fluxes from ARM (for SFC) and CERES (for TOA). g-l, bar charts of standard deviation of lines in a-f. s-x, bar charts of standard deviation of lines in m-r. Black bar (O) stands for standard deviation of observed total-sky SW flux anomalies from ARM or CERES, red for water vapor kernel-estimated changes in SW fluxes, blue for surface albedo kernel-estimated changes, and orange for cloud kernel-estimated changes.

**Figure 6.** Decomposition of monthly kernel-estimated changes in **ARM** total-sky LW fluxes at SFC (a-f) and TOA (m-r) into LW water vapor (red), air temperature (blue), surface temperature (green), and cloud (orange) kernel-estimated changes for the six ARM sites. These kernel-estimated responses are calculated using **ARM-observed** water vapor and air and surface temperature. Black line represents monthly anomalies of observed total-sky LW fluxes from ARM (for SFC) and CERES (for TOA). g-l, bar charts of standard deviation of lines in a-f. s-x, bar charts of standard deviation of lines in m-r. Black bar (O) stands for standard deviation of observed total-sky LW flux anomalies from ARM or CERES, red for water vapor kernel-estimated changes in LW fluxes, blue for surface albedo kernel-estimated changes, and orange for cloud kernel-estimated changes.

**Figure 7.** Comparison of vertical profiles of water vapor (WV) and temperature (T) kernel-estimated changes in clear-sky SW and LW fluxes (unit:  $\text{W/m}^2$ ) calculated using ARM

(red) and ERA5 (blue) state variables at SFC and TOA for the six ARM sites. The red and blue lines are the average of water vapor or temperature kernel responses over the chosen period in Fig. 1; the red and blue shades represent the standard deviation of the kernel responses during the period.

**Evaluation of CloudSat Radiative Kernels Using ARM and CERES Observations and ERA5 Reanalysis**

Ni Dai<sup>1\*</sup>, Ryan J. Kramer<sup>2,3</sup>, Brian J. Soden<sup>4</sup>, and Tristan S. L'Ecuyer<sup>5</sup>

<sup>1</sup>*Joint Institute for Regional Earth System Science & Engineering, University of California, Los Angeles, Los Angeles, CA, 90095, USA*

<sup>2</sup>*Climate and Radiation Laboratory, Earth Sciences Division, NASA Goddard Space Flight Center, Greenbelt, MD, 20771, USA*

<sup>3</sup>*Joint Center for Earth Systems Technology, University of Maryland at Baltimore County, Baltimore, MD, USA*

<sup>4</sup>*Rosenstiel School of Marine and Atmospheric Sciences, University of Miami, Miami, FL, 33149, USA*

<sup>5</sup>*Department of Atmospheric and Oceanic Sciences, University of Wisconsin-Madison, Madison, WI, 53706, USA*

*\*Corresponding author address: Ni Dai, Joint Institute for Regional Earth System Science & Engineering, University of California, 4242 Young Hall, Los Angeles, CA, 90095, USA*

*E-mail: ndai@umd.edu*

**Key points**

- Observation-based CloudSat radiative kernels are evaluated with field observations for six ARM sites with different climate characteristics.

- The kernels are found to be valuable for reconstructing observed radiative flux anomalies at the surface and top-of-atmosphere.
- The CloudSat kernels are the least skilled in reconstructing the observed changes in longwave radiative flux at the surface.

## **Abstract**

Despite the widespread use of the radiative kernel technique for studying radiative feedbacks and radiative forcings, there has not been any systematic, observation-based validation of the radiative kernel method. Here, we utilize observed and reanalyzed radiative fluxes and atmospheric profiles from the Atmospheric Radiation Measurement (ARM) program and ERA5 reanalysis to assess a set of observation-based radiative kernels from CloudSat for six ARM sites. The CloudSat radiative kernels, convoluted with the ERA5 state variables, can almost perfectly reconstruct the monthly anomalies of shortwave (SW) and longwave (LW) radiative fluxes in ERA5 at the surface (SFC) and top-of-atmosphere (TOA) with correlations significantly being greater than 0.95. The biases of kernel-estimated flux anomalies calculated using the ARM-observed state variables can be more than twice as large when compared with the ARM-observed surface flux anomalies and Clouds and Earth's Radiant Energy System (CERES) observed anomalies at the TOA. Generally, clouds contribute to most (>60%) of the variance of flux anomalies at Southern Great Plain (SGP), Tropical Western Pacific (TWP), and Eastern North Atlantic (ENA), and surface albedo dominates (>69%) the variance of SW flux anomalies at North Slope of Alaska (NSA). The radiative kernels exhibit the lowest correlation ( $r \sim [0.55, 0.85]$ ) when reconstructing SFC LW flux anomalies at SGP, TWP, and ENA, whose biases are related

to the possibility that the kernels may not fully capture the characteristics associated with MJO and ENSO at TWP and the presence of clouds at SGP and ENA.

## 1. Introduction

In radiative equilibrium over sufficiently long time scales, radiative forcing, the difference between incoming and outgoing radiation, is balanced by amplified or dampened responses in radiative fluxes due directly or indirectly to forced changes in temperature – a process known as radiative feedback. The radiative feedbacks can be separated into contributions from the atmosphere and surface temperature, water vapor, cloud, and surface albedo (Soden and Held 2006). Uncertainty relevant to these feedbacks, particularly the cloud feedback, exists in current global climate models (GCMs) and is the main cause of intermodel differences in estimating the equilibrium climate sensitivity (e.g., Bony et al. 2006; Dufresne and Bony 2008; Vial et al. 2013; Zelinka et al. 2020).

The radiative kernel technique (Soden and Held 2006) is extensively used to isolate and quantify a radiative feedback or changes in radiative fluxes at the surface (SFC) and top-of-atmosphere (TOA) caused by a certain atmospheric or surface variable. A radiative kernel is commonly generated by computing the differential radiative response ( $K^x = \frac{\partial R}{\partial x}$ ) of the radiative flux ( $R$ ) at the SFC or TOA to a small perturbation of a state variable  $x$  (e.g. temperature, water vapor, and surface albedo) based on a radiative transfer model and the climatological base state. Multiplying the kernel with the climate response of the variable ( $\frac{\partial x}{\partial T}$ , where  $T$  is the surface air temperature) or the perturbation in the variable itself

( $\delta x = x^B - x^A$ , where A and B represent two different atmospheric states in equilibrium)  
quantifies the radiative feedback ( $\frac{\partial R}{\partial T}$ ) or the changes in flux due to the perturbation ( $\delta R$ ).

The climatological base state used for the kernel calculation usually comes from a GCM or a GCM-based reanalysis. A GCM represents a global climate system that approximately satisfying the conservation laws of momentum, mass, and energy, and therefore is a great tool to estimate radiative feedbacks in idealized experiments and future projections. The TOA-based kernels were first calculated with the GFDL model (Soden and Held 2006; Soden et al. 2008). Since then, the simplicity of the radiative kernel technique and its easy application across different GCMs have encouraged many other versions of kernels. The SFC or TOA-based kernels have been generated with CAM3 (Shell et al. 2008), ECHAM5 (Previdi, 2010), MPI-ESM-LR (Block and Mauritsen 2013), CESM-CAM5 (Pendergrass et al. 2018) model, and among others, as well as the ERA-Interim and RRTM reanalysis (Huang et al. 2017). The kernel technique has also been adapted for a better separation of individual feedbacks (Held and Shell 2012; Block and Mauritsen 2013), for simulations with large forcings or perturbations (Jonko et al. 2012; Sanderson and Shell 2012), and for computing cloud feedbacks (Zelinka et al. 2012a).

However, the GCM-based radiative kernels are susceptible to systematic biases and limitations associated with the model-derived climatological base state, which can lead to uncertainty in the estimation of radiative feedbacks. For example, differences in the approximate parameterization of horizontal and vertical cloud distribution among GCMs can contribute to differences in the kernel calculation (Kramer et al. 2019). When applying these GCM-based kernels to present-day climate, the biases of the kernel-estimated radiative feedbacks and changes in radiative fluxes can be amplified by large differences

between the model-derived base state and the observed climatology due to the assumption of linearity between the radiative fluxes and the state variables in the kernel calculation (Jonko et al. 2012; Block and Mauritsen 2013).

Radiative kernels derived directly from observations are independent of the GCM-based biases and are better suited for understanding changes in radiative fluxes within the modes of natural climate variabilities. For example, Berry et al. (2020) created cloud radiative kernels from A-Train over the Eastern Pacific to examine liquid clouds in CAM5. Kramer et al. (2019) developed a set of observation-based radiative kernels using the CloudSat level-2B atmospheric fluxes and heating rate product (2B-FLXHR-LIDAR; Matus & L'Ecuyer 2017). Their approach to derive the satellite-based CloudSat kernels is similar to the process of generating GCM-based kernels. They recomputed atmospheric instantaneous fluxes in both clear and cloudy skies using the 2B-FLXHR-LIDAR algorithm initialized with the profiles of cloud information from CloudSat/CALIPSO and the state variables (temperature, water vapor, and surface albedo) and derived the 12-month radiative kernels from the differences between the fluxes with and without perturbation.

Although these observation-based radiative kernels are ideal for evaluating radiative feedbacks in GCMs and estimating radiative feedbacks or changes in radiative fluxes due to natural climate variability, they could still be susceptible to a variety of errors. For example, the 12-month CloudSat radiative kernels are only based on one year of data from 2009 since the kernel calculation is computationally expensive (Pendergrass et al. 2018). Therefore, they do not represent the internal interannual variability. According to Kramer et al. (2019), interannual variability is a relatively small source for radiative kernel error globally and zonally, but the errors are larger locally, especially in regions where the

radiative kernel is small. Given the fact that the CloudSat 2B-FLXHR-LIDAR product does not capture the diurnal cycle, does not resolve spatial scales less than 1km, and typically cannot discern precipitation from clouds, the related errors/uncertainty may show up as a residual in the monthly-averaged CloudSat kernels. Additionally, since the CloudSat radiative kernels rely on a radiative transfer model, they may be subject to radiative transfer errors, which has led to differences in SFC-based GCM radiative kernels (Kramer et al. 2019).

The exercise of validating the observation-based CloudSat radiative kernels with reanalyses and observations is a worthwhile one. Here, we assess satellite-based radiative kernels using observed and reanalyzed broadband longwave (LW) and shortwave (SW) fluxes and atmospheric profiles from the Atmospheric Radiation Measurement (ARM) program (Stokes and Schwartz 1994; Ackerman and Stokes 2003; Ellingson et al. 2016, chapter 1; Stokes 2016, chapter 2) and ERA5 reanalysis at four different research facilities (with a total of six sites) located in Southern Great Plains, North Slope of Alaska, Tropical Western Pacific, and Eastern North Atlantic. These facilities are under a variety of climate conditions, whose observations offer a unique resource to evaluate the CloudSat kernels and the decomposition of changes in fluxes using these kernels. Since the ARM sites only provide observed radiative fluxes at the SFC, we employ the co-located satellite-based clear-sky TOA fluxes from Clouds and Earth's Radiant Energy System (CERES) to assess the TOA radiative kernels. Following the approach in Huang et al. (2007), monthly anomalies of the observed or reanalyzed profiles of atmospheric temperature and humidity together with estimated surface albedo are convolved with the SFC and TOA CloudSat radiative kernels to produce the kernel-estimated changes in SFC and TOA fluxes, which



are then compared with the flux anomalies from ARM/CERES or the ERA5 reanalysis. In addition, we identify the contribution from each kernel state variable to the changes in radiative fluxes at each ARM site and investigate the potential sources of bias in these kernel-estimated changes.

## **2. Data**

### **2.1 Observation-Based Radiative kernels from CloudSat/CALIPSO**

The total-sky and clear-sky CloudSat radiative kernels for perturbations of the air and surface temperature, water vapor, and surface albedo are based on the TOA and SFC broadband LW and SW fluxes from CloudSat 2B-FLXHR-LIDAR fluxes and heating rate product (Matus & L'Ecuyer 2017). Following Soden et al. (2008), Kramer et al. (2019) perturbed the inputs (including the temperature, humidity, surface albedo, and profiles of cloud information) to the 2B-FLXHR-LIDAR algorithm (Henderson et al. 2013) to derive perturbed TOA and SFC CloudSat fluxes at each horizontal point corresponding to a 1K increase in temperature, a 1% increase in surface albedo, and an increase in specific humidity corresponding to a 1K warming at fixed relative humidity. The temperature and humidity profiles were from the CloudSat ECMWF-AUX data product, which is customized from the AN-ECMWF dataset (provided by the European Center for Medium-Range Weather Forecasts) by setting to the time and location of each Cloudsat footprint. Surface albedo is from the CloudSat ancillary albedo product based on the International Geosphere-Biosphere Programme global land surface classification. The profiles of cloud information include cloud liquid water content and ice water content from the CloudSat

2B-CWC product and Cloud layers and their heights from the combined CloudSat and CALIPSO product (Henderson et al. 2013).

The radiative kernels for each atmospheric state variable were generated from the differences between the perturbed fluxes and those from the standard 2B-FLXHR-LIDAR calculation without any perturbed variables. Additional details can be found in Kramer et al. (2019) and Henderson et al. (2013). The 12-monthly mean radiative kernels used in this study are archived on a  $2^{\circ} \times 2.5^{\circ}$  global grid and 30 sigma vertical levels. For each ARM site, the radiative kernels at the nearest grid point to the actual location of that ARM site are used.

## **2.2 ARM data**

The four primary ARM sites considered in this study are: the Southern Great Plains (SGP; Sisterson et al. 2016) centered at  $36.6^{\circ}\text{N}$ ,  $97.5^{\circ}\text{W}$  (near Lamont, Oklahoma, United States), the North Slope of Alaska (NSA; Verlinde et al. 2016) at  $71.3^{\circ}\text{N}$ ,  $156.6^{\circ}\text{W}$  (Barrow, Alaska, United States), the Tropical Western Pacific (TWP C1; Long et al. 2016) at  $2.0^{\circ}\text{S}$ ,  $147.4^{\circ}\text{E}$  (Manus Island, Papua New Guinea), and the Eastern North Atlantic (ENA C1) site at  $39.1^{\circ}\text{N}$ ,  $28^{\circ}\text{W}$  (Graciosa Island in the Azores archipelago). TWP field sites at  $0.5^{\circ}\text{S}$ ,  $166.9^{\circ}\text{E}$  (TWP C2; Nauru Island, Republic of Nauru) and  $12.4^{\circ}\text{S}$ ,  $130.9^{\circ}\text{E}$  (TWP C3; Darwin, Australia) are also included. The facility operations and data collections began in 1993 for SGP, 1997 for NSA, 1996 for TWP, and 2013 for ENA. Operations and data collections for the three TWP sites ended in 2014. Each of these six sites consists of a multitude of instruments, including the millimeter-wavelength cloud radar, Raman lidar, broadband radiometers, aerosol observing systems, and balloon-borne radiosondes. These

observing systems routinely measure vertical profiles of clouds and their optical properties as well as the atmospheric profiles of temperature and humidity.

### **2.2.1 Observed SFC radiative fluxes from ARM Radiative Flux Analysis (RFA)**

We extract the total-sky and clear-sky downwelling and upwelling SFC SW fluxes and downwelling SFC LW flux from the quality-controlled ARM RFA value-added product (ARM 2020). The clear-sky fluxes are estimated from the algorithms for detecting clear skies and fitting clear-sky SW and LW functions, which are described in Long and Ackerman (2000) and (2008). The estimated uncertainty for total-sky surface downwelling SW and LW irradiance measurement is 6% or  $10 \text{ W m}^{-2}$  (whichever is larger) and 2.5% or  $4 \text{ W m}^{-2}$  (Stoffel 2005). The root-mean-square error (RMSE) of clear-sky fluxes approximately doubles the measurement uncertainty of the total-sky ones. These estimates begin from September 2003 and end between 2013 and 2017 for the SGP, NSA, and TWP sites, and from February 2013 to October 2019 for the ENA site. They are archived on a temporal resolution of one minute and have been averaged to hourly data. For the total-sky fluxes in this study, only measurements that passed quality control tests are considered.

### **2.2.2 Temperature and humidity products from ARMBEATM**

ARM Best Estimate (ARMBE; Xie et al. 2010) is a summary product of many ARM observations and is designed for climate model evaluation. This value-added product merges data from a variety of ARM instruments, performs quality control checks, and averages parameters to a temporal resolution of one hour. The ARM atmospheric measurements of interest in this study are the hourly surface and air temperature (K) and relative humidity (%) from the subset of ARM Best Estimate Atmospheric Measurement (ARMBEATM) with a period of January 1998 - December 2011 for SGP, January 1998 –

December 2010 for the NSA and TWP sites, and January 2014 – December 2018 for ENA. Note that valid ARMBEATM measurements of air temperature and relative humidity are archived only on a few hours (of the daily standard 24 hours) each day and may not fully represent the diurnal cycle. The hours can be different for different ARM sites. To minimize the potential impact of diurnal variation, we choose those hours with the largest number of valid measurements of non-zero temperature and relative humidity according to a composite distribution (not shown) of the 24-hour diurnal cycle: 6:00, 12:00, 18:00, and 24:00 for the SGP site; 6:00, 18:00, and 24:00 for NSA; 12:00 and 24:00 for TWP C1, C2, and C3; and 6:00, 12:00, 18:00, and 24:00 for ENA. The total samples of valid and non-zero observations for each site can be found in Table S1. At SGP C1, TWP C1, TWP C3, and ENA C1, the percentage differences among the number of samples of the selected hours are very small (Table S1) and thus the impact of diurnal variation can be neglected for these four sites. For NSA C1 and TWP C1, on average, a certain hour can have 3.8 (at NSA C1) and 1.6 (at TWP C1) more samples than the other hours per month. Even though, the potential impact of diurnal variation due to such a sampling bias of the monthly-averaged air temperature or relative humidity should be small at these two sites. The ARMBEATM product does not include uncertainty estimates on the data values. According to Climate Science for a Sustainable Energy Future Atmospheric Radiation Measurement Best Estimate (CSSEFARMBE; Riihimaki et al. 2012), the uncertainty of surface temperature at SGP C1 is 0.29 K and surface relative humidity is 1.52%.

### **2.3 Observed TOA radiative fluxes from Clouds and Earth's Radiant Energy System (CERES)**

For total-sky and clear-sky TOA fluxes, we use the hourly-averaged observed fluxes from the CERES (Wielicki et al. 1996) Synoptic 1° (SYN1deg-1Hour Edition4.1; Doelling et al. 2016) product. The CERES instruments are presently flying on National Aeronautics and Space Administration (NASA)'s Terra, Aqua, and Suomi-National Polar-Orbiting Partnership satellites. The CERES observed total-sky fluxes are derived by combining Terra and Aqua CERES-observed temporally interpolated TOA radiative fluxes. Hourly radiances from geostationary (GEO) imagers are converted to broadband GEO TOA fluxes via empirical regression and angular distribution models (Loeb et al. 2005), which are used to more accurately model the variability between CERES observations. The CERES/GEO flux observations are spatially averaged into 1° gridded regions. Clear-sky fluxes are computed hourly for each 1° gridded region by removing clouds based on the CERES project's Moderate Resolution Imaging Spectroradiometer (MODIS) imager cloud retrievals (Minnis et al. 2011). The hourly CERES SYN1deg product is archived on a 1°×1° global grid from March 2003 to the present. In this study, the total-sky and clear-sky TOA fluxes at the nearest grid point to the actual location of each ARM site represent the TOA fluxes used for that ARM site.

## **2.4 ERA5 Reanalysis**

The ERA5 reanalysis (Hersbach et al. 2020) is a state-of-the-art global atmospheric reanalysis produced by the European Centre for Medium-Range Weather Forecasts (ECMWF). It replaces its predecessor ERA-Interim (Dee et al. 2011). This dataset is archived on a global grid with a very high spatial resolution ( $0.25^\circ \times 0.25^\circ$ ) and 37 pressure levels, currently available for January 1979 to the present. The hourly model output of ERA5 is generated by an operational Integrated Forecast System (IFS CY41r2) with TL639

spectral resolution (31km) and 137 vertical levels up to 0.01 hPa. This system uses a 12-hourly ensemble-based 4-dimensional variational assimilation (4D-Var ensemble) that enables improved analyses by assimilating the model forecast fields, vast amounts of historical satellite and in-situ observations, and forcings from the improved radiation system and sea-surface boundary conditions. The biases of satellite-measured radiance and ground-based radar-gauge composites, total column ozone, aircraft temperature, and surface pressure observations are automatically corrected via a variational bias correction scheme. Additional information can be found on the ERA5 website (<https://www.ecmwf.int/en/forecasts/datasets/reanalysis-datasets/era5>). The ERA5 outputs used in this study are monthly-averaged surface and air temperature, relative humidity, and total-sky and clear-sky SW and LW fluxes at the SFC and TOA. As noted in Section 2.1, the temperature and humidity profiles used to calculate fluxes in the 2B-FLXHR-LIDAR algorithm came from the ECMWF-based analyses. Therefore, it is particularly relevant to use ERA5 for this study, assuming the ECMWF product in 2B-FLXHR-LIDAR and ERA5 are similar. The ERA5 surface albedo is defined as monthly upwelling surface clear-sky flux divided by monthly downwelling surface clear-sky flux. To be compared with the ARM observations, the ERA5 fluxes and state variables are area-averaged over a  $5^{\circ} \times 5^{\circ}$  domain with the nearest grid point to the actual location of each ARM site being at the center.

### **3. Methodology**

#### **3.1 Monthly flux anomalies from ARM, CERES and ERA5**

The monthly-averaged fluxes of ERA5 are directly downloaded from the ERA5 website and are averaged using all the daily 24 hours to incorporate the full diurnal cycle. The flux anomalies are computed by subtracting the monthly flux climatology of the period of April 2006 – September 2009 (January 2014 – December 2018) from the monthly-averaged flux for the SGP, NSA, and TWP sites (the ENA site).

To calculate the monthly anomalies of SFC fluxes from ARM and TOA fluxes from CERES, we first compute daily averaged fluxes based on those selected hours of air temperature and relative humidity from ARMBEATM described in Section 2.1. Monthly-averaged fluxes are averaged from these daily ones. Only those months with more than 20 days of valid data for each selected hour are considered in this study. Monthly flux anomalies of ARM and CERES are calculated by subtracting the monthly flux climatology of the period of April 2006 – September 2009 (January 2014 – December 2018) from the monthly-averaged flux for the SGP, NSA, and TWP sites (the ENA site).

### 3.2 Monthly kernel-estimated changes in radiative fluxes

Following Huang et al. (2007) and Soden et al. (2008), the monthly kernel-estimated changes in total-sky LW flux at the SFC or TOA can be expressed as:

$$\Delta LW = \Delta R_{C(LW)} + \sum_i K_{T_a(LW)}^i \Delta T_a^i + \sum_i K_{\omega(LW)}^i \Delta \omega^i + K_{T_s(LW)} \Delta T_s \quad (1)$$

$\Delta R_{C(LW)}$  is the LW cloud variability term in this study, defined as:

$$\begin{aligned} \Delta R_{C(LW)} = & \Delta LW^* - \Delta LW_0^* - \sum_i (K_{T_a(LW)}^i - K_{0T_a(LW)}^i) \Delta T_a^i - \\ & \sum_i (K_{\omega(LW)}^i - K_{0\omega(LW)}^i) \Delta \omega^i - (K_{T_s(LW)} - K_{0T_s(LW)}) \Delta T_s \end{aligned} \quad (2)$$

in which  $\Delta LW_0^*$  stands for observed or reanalyzed clear-sky LW flux and  $\Delta LW^*$  for observed or reanalyzed total-sky LW flux.  $\Delta LW^* - \Delta LW_0^*$  equals the changes in LW

cloud radiative effect (dCRE; Cess et al. 1990). In both equation (1) and (2),  $i$  is an index of vertical levels,  $K_{T_a(LW)}$  for the total-sky LW air temperature kernel ( $\text{W/m}^2/\text{K}\cdot 100\text{hPa}$ ) from CloudSat,  $K_{\omega(LW)}$  for the total-sky LW water vapor kernel ( $\text{W/m}^2/\text{K}\cdot 100\text{hPa}$ ),  $K_{T_s(LW)}$  for the total-sky LW surface temperature kernel ( $\text{W/m}^2/\text{K}$ ),  $\Delta T_a$  for the monthly air temperature kernel input (unit in K),  $\Delta T_s$  the monthly surface temperature anomaly (unit in K), and  $\Delta\omega$  for the monthly water vapor kernel input (unit in K).  $K_{0T_a(LW)}^i$  in equation (2) stands for the clear-sky LW air temperature kernel ( $\text{W/m}^2/\text{K}\cdot 100\text{hPa}$ ),  $K_{0\omega(LW)}$  for the clear-sky LW water vapor kernel ( $\text{W/m}^2/\text{K}\cdot 100\text{hPa}$ ), and  $K_{0T_s(LW)}$  for the clear-sky LW surface temperature kernel ( $\text{W/m}^2/\text{K}$ ). The  $(K_x - K_{0x})\Delta x$  term is referred to as the  $K_x$  cloud mask.

In this study,  $\Delta T_a$  and  $\Delta\omega$  are defined as below, following Sanderson and Shell (2012):

$$\Delta T_a = (T_a - \overline{T_a}) \frac{\Delta p}{100\text{hPa}} \quad (3)$$

$$\Delta\omega = \frac{\ln[w(T_a, RH)] - \ln[w(\overline{T_a}, \overline{RH})]}{\ln[w(\overline{T_a}+1, \overline{RH})] - \ln[w(\overline{T_a}, \overline{RH})]/\text{K}} \frac{\Delta p}{100\text{hPa}} \quad (4)$$

$T_a$  is monthly air temperature, RH the relative humidity, and  $w$  the specific humidity calculated using the air temperature and relative humidity in brackets. The overbar represents the monthly climatology. The division by K in the denominator of the term  $\frac{\ln[w(T_a, RH)] - \ln[w(\overline{T_a}, \overline{RH})]}{\ln[w(\overline{T_a}+1, \overline{RH})] - \ln[w(\overline{T_a}, \overline{RH})]/\text{K}}$  means that this term has a unit of Kelvin. Monthly-averaged air temperature or relative humidity of ARM are computed from the daily average of air temperature or relative humidity of the selected hours described in Section 2.1. For ERA5, the monthly temperature and humidity are averaged for the daily 24 hours.



316 Similarly, the kernel-estimated changes of total-sky SW fluxes at the SFC or TOA  
 317 can be written as:

$$318 \quad \Delta SW = \Delta R_{C(SW)} + \sum_i K_{\omega(SW)}^i \Delta \omega^i + K_{\alpha(SW)} \Delta \alpha \quad (5)$$

319  $\Delta R_{C(SW)}$  is the SW cloud variability term, defined as:

$$320 \quad \Delta R_{C(SW)} = \Delta SW^* - \Delta SW_0^* - \sum_i (K_{\omega(SW)}^i - K_{0\omega(SW)}^i) \Delta \omega^i - (K_{\alpha(SW)} - K_{0\alpha(SW)}) \Delta \alpha \quad (6)$$

321 where  $\Delta SW_0^*$  stands for observed or reanalyzed clear-sky SW flux and  $\Delta SW^*$  for observed  
 322 or reanalyzed total-sky SW flux.  $\Delta SW^* - \Delta SW_0^*$  equals the changes in SW dCRE.  $K_{\omega(SW)}^i$   
 323 here is the total-sky SW water vapor kernel (W/m<sup>2</sup>/K·100hPa),  $K_{\alpha(SW)}$  the total-sky surface  
 324 albedo kernel (W/m<sup>2</sup>/%),  $K_{0\omega(SW)}^i$  here is the clear-sky SW water vapor kernel  
 325 (W/m<sup>2</sup>/K·100hPa),  $K_{0\alpha(SW)}$  the clear-sky surface albedo kernel (W/m<sup>2</sup>/%),  $\Delta \alpha$  the monthly  
 326 surface albedo anomaly (%) and  $\Delta \omega$  is from equation (4). The monthly surface albedo is  
 327 defined as monthly upwelling surface clear-sky flux divided by downwelling surface clear-  
 328 sky flux. Monthly-averaged surface albedo of ARM and CERES is computed based on the  
 329 daily average of selected hours described in Section 2.1.

330 The monthly clear-sky kernel-estimated changes in LW and SW fluxes at the SFC  
 331 or TOA can be expressed as:

$$332 \quad \Delta LW_0 = \sum_i K_{0T_a(LW)}^i \Delta T_a^i + \sum_i K_{0\omega(LW)}^i \Delta \omega^i + K_{0T_s(LW)} \Delta T_s \quad (7)$$

$$333 \quad \Delta SW_0 = \sum_i K_{0\omega(SW)}^i \Delta \omega^i + K_{0\alpha(SW)} \Delta \alpha \quad (8)$$

334 Note that we do not account for the instantaneous radiative forcing (IRF) in the  
 335 calculation of the kernel-estimated changes in the total-sky and clear-sky SW and LW  
 336 fluxes in equations (1), (5), and (7)-(8). The common approach to diagnose IRF is to  
 337 subtract the sum of kernel-derived state-variable-dependent flux anomalies (e.g.,  $\Delta LW$  in

equation (1) and  $\Delta SW$  in equation (5)) from the total flux anomalies (e.g., from CERES or ARM). Adding the IRF to equations (1), (5), and (7)-(8) will result in the actual total flux anomalies and does not contribute to our goal of comparing these two sets of flux anomalies. In addition, the IRF plays a secondary role in the interannual variability of the observed TOA CERES fluxes, compared with the kernel-estimated radiative responses during 2003-2018 (Kramer et al. 2021).

## **4. Results**

### **4.1 Validation of CloudSat kernels with ERA5 reanalysis**

The CloudSat radiative kernels are first assessed with the spatially and temporally consistent ERA5 reanalysis products before the approximate decomposition of the contributions to changes in ARM/CERES-observed radiative fluxes. The GCM-based ERA5 reanalysis combines an abundance of observations and measurements with model information and provides a dynamically and thermodynamically consistent estimate of the global climate state at each hourly time step. Its high spatial resolution of  $0.25^\circ \times 0.25^\circ$  means that the distance between the closest grid point to an ARM site and the actual location of that ARM site is less than 50km. One caveat of using the ERA5 reanalysis here is that the potential changes in assimilated observations can produce artificial variability in the ERA5 kernel-estimated changes in fluxes.

Monthly kernel-estimated changes in total-sky SW and LW fluxes calculated using the ERA5 state variables are shown in Fig. 1 and 2 for the six ARM sites: SGP C1, NSA C1, TWP C1, TWP C2, TWP C3, and ENA C1. Table 1 documents the mean absolute bias (Abs Bias), root mean square error (RMSE), RMSE normalized by the standard deviation

of the monthly anomalies of ERA5 fluxes (RMSE\*), and correlation coefficient of these kernel-estimated changes in comparison with the monthly anomalies of SW and LW fluxes obtained from ERA5. Note, the Abs Bias and RMSE of the total-sky SW and LW flux results are equal to those of the clear-sky SW and LW flux ones in Table S2. When equation (2) is substituted in equation (1), the error of kernel-estimated total-sky flux anomalies is identical to the one of kernel-estimated clear-sky flux anomalies. The correlation coefficients of the total-sky and clear-sky results can be different, which measure how well the kernel-estimated flux anomalies co-vary with the reanalyzed/observed flux anomalies.

To understand how using only one year (the Year 2009 in this study) of radiative kernels impacts the biases of multi-year kernel-estimated flux anomalies, which stems from the inability of these kernels to represent the interannual variability, we show the maximum RMSE as a function of the average length (ranging from one month to multiple years) for each site in Fig. S1. Overall, for the lengths that are longer than 13 months, the maximum RMSE decreases as the length of months increases. This implies that the biases related to using only one year of kernels can be reduced if longer periods are used to compare the kernel-estimated flux anomalies with the observed or reanalyzed ones. However, Fig. S1 exhibits that the RMSEs of the Year 2009 still tend to be smaller than those of the period of 09/2003-12/2010. The percentage errors of Abs Bias and RMSE from the Abs Bias or RMSE for the Year 2009 are shown in Table 1.

#### **4.1.1 SGP C1**

Located in the midlatitude and mid-continent, ARM SGP is the largest and most extensive climate research field facility in the world. This central site (SGP C1) experiences large seasonal variations in both temperature and humidity and a great range

of surface energy fluxes and cloud properties. Fig. 1a&g, Fig. 2a&g, Table 1, and Table S2 show that the kernel-estimated changes in both total-sky and clear-sky SW and LW fluxes calculated with the ERA5 state variables are highly correlated ( $r > 0.9$  at a significance level of 99%) with the monthly anomalies of ERA5 fluxes at the SFC and TOA and in the atmospheric column (ATM, equaling to TOA minus SFC). The RMSEs of SW and LW fluxes are smaller than  $2.6 \text{ W/m}^2$ . The relatively small percentage errors from the Year 2009 (Table 1 and Fig. S1) suggest that the lack of kernel interannual variability representation is not a significant contributing factor to the kernel-estimated errors of SW and LW flux anomalies at the SFC and TOA at SGP C1.

#### **4.1.2 NSA C1**

The NSA central site is located at the edge of the Arctic Ocean, where the sea ice, land ice, and permafrost are highly sensitive to the changes in energy fluxes. The climate at NSA is characterized by low temperatures and low humidity. Most Arctic clouds are found in the lower troposphere, where they interact with strong near-surface temperature inversions. Due to very small insolation during the northern hemisphere winter season at NSA, the changes in SW fluxes are near zero during winter and only become large in summer. The kernel-estimated changes in total-sky and clear-sky SW fluxes at the SFC and TOA show almost perfect agreement with the ERA5 SW flux anomalies ( $r \geq 0.99$ ; Fig. 1b&h, Table 1, and Table S2). For total-sky LW fluxes, the kernel-estimated changes exhibit a lower correlation with the ERA5 LW flux anomalies ( $r \leq 0.81$ ; Table 1). The correlation of kernel-estimated changes in clear-sky LW fluxes is even lower (Table S2), suggesting that the water vapor or temperature-related changes could contribute more to the bias than the cloud-related ones. Similar to the SGP results, the lack of kernel

interannual variability representation seems to not contribute much to the kernel-estimated errors at NSA (Table 1 and Fig. S1).

#### **4.1.3 Three TWP sites**

The three TWP sites are located in the tropical western Pacific region roughly 2000km apart. According to Long et al. (2016), the TWP C1 site (Manus) primarily experiences an oceanic climate, whose variability of convective activities is driven by the Madden-Julian oscillation (MJO; Madden and Julian 1994). The TWP C2 site (Nauru) is strongly influenced by the variability associated with El Niño-Southern Oscillation (ENSO). The convection and cloudiness over this site are enhanced during El Niño events and suppressed during La Niña events. Fig. 1d and Fig. 2d exhibit an increase of SFC SW flux anomalies and a decrease of SFC LW flux anomalies during the 2008-2009 and 2010-2011 La Niña events, corresponding to a reduction of convective activities during these periods. TWP C3 (Darwin) is a coastal site. Rather than being driven by land-sea circulations and associated coastal convection, the convection over TWP C3 is dominated by the annual Australian monsoon. For the total-sky results, the kernel-estimated changes in both SW and LW radiative fluxes at the three TWP sites almost perfectly agree with the ERA5 SW and LW flux anomalies ( $r > 0.95$ ; Fig. 1&2, Table 1). The RMSEs are smaller than  $3.5 \text{ W/m}^2$ . The lack of kernel interannual variability representation contributes to the kernel-estimated errors more significantly at the three TWP sites (especially at TWP C1 and C3) than at SGP and NSA (Table 1 and Fig. S1).

#### **4.1.4 ENA C1**

The ENA site is a relatively newer ARM site and is characterized by marine stratocumulus clouds. Given the fact that low cloud radiative feedback is a leading factor

causing the large spread in equilibrium climate sensitivity (ECS) (Bony and Dufresne 2005; Andrews et al. 2012; Zelinka et al. 2012b), it is important to evaluate whether the CloudSat kernels are capable of reconstructing fluxes anomalies in the presence of boundary layer clouds. Fig. 1f&l, Fig. 2f&l, and Table 1 show that the kernel-estimated changes in total-sky SW and LW fluxes calculated with the ERA5 state variables at ENA are highly correlated ( $r > 0.95$  at a significance level of 99%) with the monthly anomalies of ERA5 total-sky fluxes at the SFC and TOA and in ATM.

Overall, these comparison results of the ERA5 flux anomalies validate that the CloudSat radiative kernels are useful to reconstruct the interannual variability in radiative fluxes for the six ARM sites. As shown in the scatterplots of Fig. 3, the kernel-estimated changes in radiative fluxes calculated with the ERA5 state variables are almost perfectly correlated with the ERA5 flux anomalies (with RMSEs being smaller than  $3.5 \text{ W/m}^2$ ), except for the kernel-estimated LW flux anomalies at NSA. Note, the 2B-FLXHR-LIDAR used to develop the CloudSat kernels incorporate temperature and humidity profiles from a product similar to ERA5, which could also contribute to the strong correlations in these ERA5 results, specifically. The kernel-estimated changes in SW fluxes exhibit smaller RMSE and higher correlation than in LW fluxes (Table 1).

#### **4.2 Evaluation of CloudSat kernels with ARM and CERES observations**

Compared with the ERA5 scatterplots in Fig. 3, the scatterplots of kernel-estimated changes in total-sky radiative fluxes calculated using ARM observed state variables versus the ARM/CERES-observed flux anomalies (Fig. 4) look more scattered. Table 2 also shows lower correlation coefficients than Table 1 in most cases. The normalized RMSEs

of the ARM kernel-estimated changes in fluxes are generally more than twice as large compared to the ERA5-based values. These results indicate that the CloudSat radiative kernels are less skilled in reconstructing observed changes in radiative fluxes at some locations than others. In this section, we also present the contribution to the changes in radiative fluxes from each state variable (shown as the standard deviation; Table 3).

#### 4.2.1 SGP C1

At SGP, the ARM kernel-estimated changes in total-sky SW and LW fluxes at the SFC and TOA (Fig. S2a&g and S3a&g) show a strong correlation ( $r > 0.9$ ) with the ARM/CERES-observed flux anomalies (Table 2), except for LW flux at the SFC ( $r \sim 0.72$ ). For SW fluxes, the changes associated with clouds dominate the kernel-estimated changes at both the SFC and TOA (Fig. 5a&m), with a standard deviation being comparable with one of the ARM/CERES-observed flux anomalies (Table 3). Surface albedo plays the second most important role in these changes, followed by water vapor. On closer inspection, dCRE (Fig. S4) accounts for most changes of the cloud-related flux anomalies rather than the SW cloud mask terms. These aforementioned SW results are similar to the ERA5 ones in Fig. S5, Fig. S6, and Table S3, indicating that the differences between the kernel-estimated and observed changes in the total-sky SW fluxes at SPG are a result of dCRE and surface albedo-related kernel-estimated changes.

Regarding the total-sky LW fluxes, the ARM/CERES results (Fig. 6, Fig. S7, and Table 3) resemble the ERA5 ones in Fig. S8, Fig. S9, and Table S3. Clouds still contribute the most to the kernel-estimated anomalies at both SFC and TOA and dCRE dominates the cloud-related changes in total-sky LW flux anomalies. However, as the correlation between the ARM-estimated clear-sky LW flux anomalies and kernel-estimated changes in clear-

sky LW flux at the SFC is also not high ( $r \sim 0.71$ ; Table S4), the bias of the kernel-estimated changes in SFC LW flux are also related to the temperature- or humidity-related kernel responses besides the cloud mask.

#### 4.2.2 NSA C1

Table 2 exhibits a high correlation ( $r > 0.9$ ) between ARM kernel-estimated changes in total-sky SW fluxes and the ARM/CERES-observed total-sky SW flux anomalies at the SFC and TOA and in ATM at NSA C1. Contrary to the ERA5-based values (Fig. S5 and Table S3), the contribution from the cloud is smaller than surface albedo in ARM/CERES (Fig. 5 and Table 3). The decomposition of the cloud-related changes in ARM/CERES-observed total-sky SW flux at the SFC (Fig. S4) shows that the variance of dCRE is larger than the one of surface albedo cloud mask. The variance of the water vapor cloud mask is almost zero. For the cloud-related changes in ARM/CERES-observed total-sky SW flux at the TOA, the variance of SW dCRE is comparable with the one of surface albedo cloud mask (Fig. S4). Both are much smaller than the variance of the observed TOA SW flux anomalies. However, the variances of ERA5 dCRE and the ERA5 TOA SW flux anomalies are much more comparable (Fig. S6).

These results suggest that the larger RMSE of the CloudSat kernels in reconstructing the observed SW flux anomalies using the ARM state variables at NSA may stem from the interannual variations in the cloud masking of the SW fluxes, which strongly depend on the covariability of clouds and surface ice and snow cover. Sledd and L'Ecuyer (2019; 2020) found that clouds have substantially reduced the ice-albedo feedback (reduction in sea ice lowers the surface albedo and increases SW absorption, which further reduces sea ice) in the Arctic by masking the effects of sea ice variability and total-sky



trends (emerged from interannual variability) in Arctic SW flux absorption take longer to detect than clear-sky trends. The precise relationship between the TOA and SFC SW fluxes and surface albedo depends critically on the cloud conditions during the years used to derive the radiative kernels. Given the fact that the CloudSat radiative kernels were derived from only one year (the Year 2009) of observation, the anomalous cloud, water vapor, snow/sea ice conditions, and their co-variations in the vicinity of the NSA site in that year may not be representative of another. Although the interannual variability seems to play an insignificant role (e.g.  $<5\%$  for SFC SW and  $<20\%$  for TOA SW) in kernel-estimated errors at NSA in ERA5 (Table 1), it actually can contribute to roughly 50% of the kernel-estimated errors in the ARM-observed results. Additionally, some complications of the interannual covariability among albedo, clouds, and radiative fluxes are not present in the reanalyses (Sledd and L'Ecuyer 2020).

For total-sky LW fluxes, adding the cloud component does not significantly affect the correlation between the changes in the ARM kernel-estimated fluxes and the ARM-observed ones (Table 2 and Table S4). Compared with the ERA5 results (Table 1) in Section 4.1.2, the ARM kernel-estimated changes in LW fluxes correlate better with the ARM/CERES-observed LW flux anomalies at the SFC and TOA and in the ATM. A similar conclusion applies to the clear-sky condition (Table S2 and Table S4). The decomposition of the kernel-estimated changes in LW fluxes (Fig. 6, Fig. S8, Table 3, and Table S3) shows that the variance of air-temperature-related changes is the largest among the four LW kernel state variables in ERA5 and much larger than the one in ARM, suggesting that the bias in air-temperature-related kernel responses may be the culprit for the low correlation in ERA5.

### 4.2.3 Three TWP sites

The ARM kernel-estimated changes in total-sky SW fluxes at these three TWP sites exhibit very a strong correlation ( $r > 0.97$ ) with the observed flux anomalies (Table 2), although the normalized RMSEs are much larger than in ERA5. Almost all of these changes are contributed from clouds (Fig. 5 and Table 3), particularly dCRE (Fig. S4). The ARM kernel-estimated responses in total-sky LW flux at the SFC exhibit moderate to high correlation, with the lowest being at TWP C1 ( $r \sim 0.55$ ) and the highest at TWP C3 ( $r \sim 0.91$ ). Unlike the ERA5 results, in which the water vapor dominates the kernel-estimated changes in total-sky SFC LW flux, the ARM results show notable contributions from surface temperature, air temperature, and clouds (particularly dCRE and water vapor cloud mask; Fig. S7), besides water vapor (Table 3). In addition, the total-sky results (Table 2) exhibits a higher correlation than the clear-sky ones (Table S4). This implies that the biases of kernel-estimated changes in SFC total-sky LW flux are related to temperature or humidity, in addition to dCRE and cloud mask. The ARM kernel-estimated changes in total-sky LW flux at the TOA correlate highly ( $r > 0.95$ ) with the CERES-observed flux anomalies (Table 2), and clouds (mostly dCRE and water vapor cloud mask) contribute the most to the changes.

### 4.2.4 ENA C1

For the ENA site, the ARM kernel-estimated changes in total-sky SW fluxes at the SFC and TOA are highly correlated ( $r > 0.98$ ) with the ARM/CERES-observed flux anomalies (Fig. S2f&l and Table 2). Similar to the SGP and TWP SW results, the majority of the kernel-estimated changes at the SFC and TOA are contributed by the cloud component (dCRE; Table 3, Table S3, Fig. 5, and Fig. S4). Even though the water vapor

546 and surface albedo-related changes in TOA SW fluxes are biased as in the clear-sky results  
547 (Table S2 and Table S4), their variances are too small to significantly lower the correlation  
548 of total-sky TOA SW fluxes (Table 3 and Table S3).

549       The comparison between the monthly anomalies of ARM-observed total-sky SFC  
550 LW flux and kernel-estimated changes in total-sky SFC LW flux shows a moderate  
551 correlation ( $r \sim 0.72$ ; Table 2). Clouds (dCRE and water vapor cloud mask) play the most  
552 important role in determining the kernel-estimated changes in LW SFC flux in both ARM  
553 and ERA5 results (Table 3, Table S3, Fig. 6, and Fig. S7). The variance associated with  
554 surface temperature is significantly larger in ARM than in ERA5 (Table 3 and Table S3).  
555 The moderate correlation indicates that the kernels might not be able to fully reconstruct  
556 the interannual variability of the observed SFC LW flux anomalies in the presence of  
557 marine boundary clouds. The ARM kernel-estimated changes in total-sky LW flux at the  
558 TOA correlate highly ( $r > 0.95$ ) with the CERES-observed flux anomalies (Table 2), and  
559 clouds (dCRE) contribute the most to the changes.

560       In summary, these results offer compelling evidence that the CloudSat radiative  
561 kernels are capable of reconstructing observed radiative fluxes anomalies at both SFC and  
562 TOA at certain ARM sites. For example, the kernel-estimated changes in SW flux at both  
563 the SFC and TOA and LW flux at the TOA exhibit a strong correlation ( $r > 0.87$ ) with the  
564 ARM and CERES flux anomalies at the SGP, NSA, TWP, and ENA sites. However, the  
565 kernels are typically less skilled in reconstructing LW flux anomalies at the SFC (e.g. low  
566 correlation coefficients in Table 2). This section also demonstrates that the CloudSat  
567 radiative kernels can be useful to separate the contribution from each state variable (water

vapor, air temperature, surface temperature, surface albedo, and clouds) to radiative flux anomalies on a local scale.

### **4.3 Bias Diagnosis**

Although the CloudSat kernels could be biased toward the ERA5 temperature and humidity profiles (e.g. the 2B-FLXHR-LIDAR used to develop the CloudSat kernels incorporate temperature and humidity profiles from a product similar to ERA5), Section 4.1 and 4.2 show that the correlations (RMSEs) between the kernel-estimated changes in LW fluxes calculated using ARM observed state variables and the ARM/CERES-observed LW flux anomalies are lower (larger) than those in ERA5, except for the LW fluxes at NSA. Given the fact that the contribution from the ARM state variables (especially water vapor and temperature) to the total kernel-estimated changes in LW flux can be different from the contribution from the ERA5 counterparts, it is important to determine whether the lower correlation in either the ARM or ERA5 results could be partially caused by the differences in their humidity and temperature profiles used to calculate the kernel-estimated changes.

Two comparisons are presented in this section. In the first comparison, we replace the ERA5 temperature and humidity used in Section 4.1 with the ARM-observed ones and seek the relationship between the monthly clear-sky flux anomalies from ERA5 and monthly clear-sky kernel-estimated changes in fluxes calculated with these ARM-observed state variables. This comparison examines the role played by the ARM-observed temperature and humidity in changing the correlation. The differences between Table S2 and Table S5 suggest the following: 1) the ARM-observed temperature and humidity at

SGP are very similar to the ERA5 ones and they do not cause much difference in correlation with and bias from the ERA5 flux anomalies; 2) the ARM observations at NSA improve the correlation with the ERA5 LW flux anomalies and lower the biases; 3) the ARM-observed water vapor and temperature profiles lower the correlation with the ERA5 SW and LW flux anomalies at the TWP and ENA sites.

The second comparison is between the monthly clear-sky flux anomalies from ARM/CERES and monthly kernel-estimated changes in clear-sky fluxes calculated with ERA5 temperature and humidity (Table S6). The ERA5 water vapor and temperature lower the correlation between kernel-estimated changes in clear-sky LW fluxes and the ARM/CERES clear-sky LW flux anomalies at NSA. We found that by using monthly ERA5 air temperature at the corresponding hours (6:00, 18:00, and 24:00) of the ARM counterparts, the monthly kernel-estimated clear-sky LW flux anomalies are much closer to the ERA5 clear-sky LW flux anomalies ( $r \sim 0.8$ ). This confirms the last statement in Section 4.2.2 that the large biases in ERA5 LW kernel responses at NSA are caused by the uncertainty associated with using diurnally-averaged air temperature from ERA5. It seems that the diurnal cycle of air temperature in the Arctic region in ERA5 may play a role in lowering the correlation of LW fluxes at NSA in ERA5. On the other hand, the ERA5 temperature and humidity profiles increase the correlation at the TWP and ENA sites, which further indicates that the CloudSat kernels could be biased towards the ERA5 temperature and humidity profiles.

In Fig. 7, we compare the vertical profiles of water vapor and air temperature kernel-estimated changes in SW and LW fluxes between ARM and ERA5 to further understand which state variable at what vertical levels is more responsible for the

differences between the ARM and ERA5 kernel-estimated changes. In general, the closer the profiles of water vapor or air temperature of ARM and ERA5 are in terms of the mean (red or blue line) and standard deviation (red or blue shade) in Fig. 7, the smaller the difference their kernel-estimated responses will be (e.g. SW fluxes at SGP, NSA, and TWP C2; see Table S2 and Table S5). For kernel-estimated LW responses at NSA, the vertical profiles of air-temperature-associated responses calculated with the ERA5 reanalysis show large differences in the lower to middle troposphere from those calculated with the ARM observations, suggesting the uncertainty in the ERA5 air temperature at these vertical levels is the culprit for causing the large biases in ERA5 LW kernel responses at this site in Section 4.1.2. At TWP C1, the lower tropospheric (middle tropospheric) water vapor and air temperature in ARM lower the correlation of ARM kernel-estimated responses in LW flux at SFC (TOA) than in ERA5. For TWP C2 (C3), the larger biases of ARM kernel-estimated responses in LW fluxes at both SFC and TOA are related to the ARM air temperature (water vapor). At ENA, since both vertical profiles of air temperature and water vapor are very similar in ARM and ERA5, the CloudSat radiative kernels cannot fully reconstruct the observed changes in LW fluxes (especially at SFC) in the presence of boundary layer clouds.

## **5. Summary**

In this study, we successfully reconstruct the monthly changes in both total-sky and clear-sky radiative fluxes in the ERA5 reanalysis and ARM/CERES observations using observation-based CloudSat radiative kernels and evaluate these kernel-estimated changes with the ERA5 and ARM/CERES flux anomalies at six ARM sites: SGP C1, NSA C1,

TWP C1, TWP C2, TWP C3, and ENA C1. Using the ERA5 state variables, the CloudSat kernels enable an almost perfect reconstruction of the changes in ERA5 total-sky SW and LW fluxes at SFC and TOA at all sites ( $r > 0.95$ ), except for the LW flux anomalies at NSA. Through a bias diagnosis, we find that the biases in the kernel-estimated changes in the LW fluxes at NSA are related to uncertainty in the diurnal cycle of the ERA5 air temperature. By replacing the ERA5 state variables with the ARM observations, the kernels demonstrate the capability to reconstruct the LW flux changes at the NSA site.

When compared with the ARM- and CERES-observed flux anomalies, the kernel-estimated changes in SW and LW fluxes calculated with the ARM-observed state variables tend to show biases that are more than twice as in ERA5. The larger biases in the ARM-observed can be explained by four possibilities: 1) the CloudSat kernels could be biased toward ERA5 as these kernels were derived using similar temperature and humidity profiles of an ECMWF product as in ERA5; 2) the better agreement in the ERA5 reanalysis could be due to the parameterizations that over-simplify relationships between clouds, local thermodynamics, and radiative fluxes; 3) there could be non-linearities or other complications in the real world that are not present in the reanalyses; 4) a  $2^\circ \times 2.5^\circ$  grid box of the CloudSat kernels where the ARM site is located may not have enough samples of the CloudSat cloud profiles within a certain month during 2009 due to the nadir view of the CloudSat observations.

The decomposition of the kernel-estimated changes in ARM-observed total-sky SW fluxes shows that the cloud component, particularly the cloud radiative effect, tends to contribute the most to the changes. For example, the CloudSat kernels cannot fully reconstruct the observed flux anomalies at NSA as complex interactions among high-

albedo snow-ice surfaces, surface-atmosphere energy and water vapor exchanges, and cloud processes are not completely understood and well parameterized (Stamnes et al. 1999).

The kernels are the least skilled in reconstructing variations in total-sky LW flux at SFC, especially at SGP C1, ENA C1, TWP C1, and TWP C2 ( $r \sim [0.55, 0.85]$ ). TWP C1, the ARM site that is most strongly influenced by MJO activities, exhibits the lowest correlation in its kernel-estimated changes in SFC LW flux than the other two TWP sites, which are characterized by the ENSO and annual Australian monsoon variability. This indicates that some environmental states during particular phases of ENSO and MJO are not well captured in the CloudSat kernels as the kernels were derived from only one year (the Year 2009) of observations. Cloud mask, temperature, and water vapor can all contribute to the biases of these ARM kernel-estimated changes in LW flux at SFC at the TWP sites. The small variance of the kernel-estimated changes in SFC LW flux also makes it difficult to discern the relative contribution from each state variable (water vapor, air temperature, surface temperature, and clouds) at TWP. The same bias diagnosis also implies that the CloudSat kernels may not be skillful enough to fully reconstruct changes in LW SFC flux in a local location that is characterized by marine boundary clouds, such as ENA, or a location with a great range of cloud properties as SGP. For LW flux at TOA, the ARM kernel-estimated changes exhibit a very high correlation with the CERES-observed anomalies, with the cloud radiative effect plays a major role in modulating these changes.

This evaluation of the observation-based CloudSat radiative kernels strengthens the confidence in estimating changes in fluxes and individual radiative feedbacks with these kernels in the present-day climate. One caveat of this study is that the kernel-estimated



changes in fluxes calculated using ARM state variables cannot capture the full diurnal cycle due to the limited sampling of the ARM air temperature and humidity. The results of both the ERA5 reanalysis and ARM observations suggest that the kernel technique is the most skilled in estimating changes in SW fluxes at both the SFC and TOA and LW flux at the TOA. Besides the aforementioned limitations of the CloudSat radiative kernels, these monthly kernels themselves can be susceptible to the sub-monthly errors/uncertainties associated with the limitations of the CloudSat/CALIPSO observation and the errors in the radiative transfer models used to generate them. However, since these errors and uncertainties have already existed in the monthly CloudSat kernels, it is not within the scope of our paper to quantify these errors. Due to the assumption of linearity between the radiative fluxes and the state variables in the kernels, the uncertainty of the kernel-estimated changes in fluxes can be amplified by any errors in the CloudSat kernels and anomalies of state variables. The CloudSat kernels considered in this study do not include any aerosol radiative effects. The direct aerosol effects, despite being a smaller influence compared to humidity and surface albedo, could still contribute to the SW flux changes (Matus et al. 2019).

## **Acknowledgment**

We would like to thank three anonymous reviewers for their helpful comments on an earlier version of the manuscript. The ARM data were obtained from the Atmospheric Radiation Measurement (ARM) user facility, a U.S. Department of Energy (DOE) office of science user facility managed by the Biological and Environmental Research Program, accessible at <https://www.arm.gov/>. The CERES flux data were obtained from the NASA Langley

Research Center Atmospheric Sciences Data Center (ASDC), accessible at  
https://ceres.larc.nasa.gov/. ERA5 reanalysis data were downloaded from the ECMWF  
Copernicus Climate Data Store (CDS), accessible at https://cds.climate.copernicus.eu/.

## References

- ARM, 2020: Radiative Flux Analysis (RADFLUX1LONG). Southern Great Plains ARM  
Data Center, accessed January 7<sup>th</sup>, 2020, <https://doi.org/10.5439/1157585>.
- Ackerman, T. P., & Stokes, G. (2003). The Atmospheric Radiation Measurement Program.  
*Phys. Today*, **56**, 38-45. doi: 10.1063/1.1554135.
- Andrews, T., Gregory, J. M., Webb, M. J., & Taylor, K. E. (2012) Forcing, feedbacks and  
climate sensitivity in CMIP5 coupled atmosphere-ocean climate models. *Geophys.*  
*Res. Lett.*, **39**, L09712, doi:10.1029/2012GL051607.
- Berry, E., Mace, G. G., & Gettelman, A. (2020). Using A-Train Observations to Evaluate  
East Pacific Cloud Occurrence and Radiative Effects in the Community Atmosphere  
Model, *Journal of Climate*, 33(14), 6187-6203. <https://doi.org/10.1175/JCLI-D-19-0870.1>
- Block, K., & Mauritsen, T. (2013). Forcing and feedback in the MPI-ESM-LR coupled  
model under abruptly quadrupled CO<sub>2</sub>. *Journal of Advances in Modeling Earth*  
*Systems*. <https://doi.org/10.1002/jame.20041>
- Bony, S., Colman, R., Kattsov, V. M., Allan, R. P., Bretherton, C. S., Dufresne, J. L., ...  
Webb, M. J. (2006). How well do we understand and evaluate climate change  
feedback processes? *Journal of Climate*. <https://doi.org/10.1175/JCLI3819.1>
- Bony, S., & Dufresne, J-L. (2005). Marine boundary layer clouds at the heart of cloud  
feedback uncertainties in climate models. *Geophys. Res. Lett.*, **32**, L20806,  
doi:10.1029/2005GL023851.
- Dee, D. P., Uppala, S. M., Simmons, A. J., Berrisford, P., Poli, P., Kobayashi, S., ... Vitart,  
F. (2011). The ERA-Interim reanalysis: Configuration and performance of the data  
assimilation system. *Quarterly Journal of the Royal Meteorological Society*.  
<https://doi.org/10.1002/qj.828>
- Doelling, D. R., Sun, M., Nguyen, L. T., Nordeen, M. L., Haney, C. O., Keyes, D. F., &  
Mlynczak, P. E. (2016). Advances in geostationary-derived longwave fluxes for the

- 739 CERES synoptic (SYN1deg) product. *Journal of Atmospheric and Oceanic*  
740 *Technology*. <https://doi.org/10.1175/JTECH-D-15-0147.1>
- 741 Dufresne, J. L., & Bony, S. (2008). An assessment of the primary sources of spread of  
742 global warming estimates from coupled atmosphere-ocean models. *Journal of*  
743 *Climate*. <https://doi.org/10.1175/2008JCLI2239.1>
- 744 Ellingson, R. G., Cess, R. D., & Potter, G. L. (2016). The Atmospheric Radiation  
745 Measurement Program: Prelude. *The Atmospheric Radiation Measurement (ARM)*  
746 *Program: The First 20 Years, Meteor. Monogr.*, No. 57, Amer. Meteor. Soc.,  
747 doi:10.1175/AMSMONOGRAPHS-D-15-0029.1.
- 748 Held, I. M., & Shell, K. M. (2012). Using relative humidity as a state variable in climate  
749 feedback analysis. *Journal of Climate*. <https://doi.org/10.1175/JCLI-D-11-00721.1>
- 750 Henderson, D. S., L'ecuyer, T., Stephens, G., Partain, P., & Sekiguchi, M. (2013). A  
751 multisensor perspective on the radiative impacts of clouds and aerosols. *Journal of*  
752 *Applied Meteorology and Climatology*. <https://doi.org/10.1175/JAMC-D-12-025.1>
- 753 Hersbach, H., Bell, B., Berrisford, P., Hirahara, S., Horányi, A., Muñoz-Sabater, J., ...  
754 Thépaut, J. N. (2020). The ERA5 global reanalysis. *Quarterly Journal of the Royal*  
755 *Meteorological Society*. <https://doi.org/10.1002/qj.3803>
- 756 Huang, Y., Ramaswamy, V., & Soden, B. (2007). An investigation of the sensitivity of the  
757 clear-sky outgoing longwave radiation to atmospheric temperature and water vapor.  
758 *Journal of Geophysical Research Atmospheres*.  
759 <https://doi.org/10.1029/2005JD006906>
- 760 Huang, Y., Xia, Y., & Tan, X. (2017). On the pattern of CO<sub>2</sub> radiative forcing and  
761 poleward energy transport. *Journal of Geophysical Research: Atmospheres*.  
762 <https://doi.org/10.1002/2017JD027221>
- 763 Jonko, A. K., Shell, K. M., Sanderson, B. M., & Danabasoglu, G. (2012). Climate  
764 Feedbacks in CCSM3 under Changing CO<sub>2</sub> forcing. Part I: Adapting the linear  
765 radiative kernel technique to feedback calculations for a broad range of forcings.  
766 *Journal of Climate*. <https://doi.org/10.1175/JCLI-D-11-00524.1>
- 767 Kramer, R. J., Matus, A. V., Soden, B. J., & L'Ecuyer, T. S. (2019). Observation-Based  
768 Radiative Kernels From CloudSat/CALIPSO. *Journal of Geophysical Research:*  
769 *Atmospheres*. <https://doi.org/10.1029/2018JD029021>
- 770 Kramer, R. J., He, H., Soden, B. J., Oreopoulos, L., Myhre, G., Forster, P. M., & Smith, C.  
771 J. (2021). Observational Evidence of Increasing Global Radiative Forcing.  
772 *Geophysical Research Letters*. 48, 7. <https://doi.org/10.1029/2020GL091585>

- 773 Loeb, N. G., Kato, S., Loukachine, K., & Manalo-Smith, N. (2005). Angular distribution  
774 models for top-of-atmosphere radiative flux estimation from the Clouds and the  
775 Earth's Radiant Energy System instrument on the Terra Satellite. Part I: Methodology.  
776 *Journal of Atmospheric and Oceanic Technology*.  
777 <https://doi.org/10.1175/JTECH1712.1>
- 778 Long, C. N., & Ackerman, T. P. (2000). Identification of clear skies from broadband  
779 pyranometer measurements and calculation of downwelling shortwave cloud effects.  
780 *Journal of Geophysical Research Atmospheres*.  
781 <https://doi.org/10.1029/2000JD900077>
- 782 Long, C. N., & Turner, D. D. (2008). A method for continuous estimation of clear-sky  
783 downwelling longwave radiative flux developed using ARM surface measurements.  
784 *Journal of Geophysical Research Atmospheres*.  
785 <https://doi.org/10.1029/2008JD009936>
- 786 Long, C. N., Mather, J. H., & Ackerman, T. P. (2016). The ARM Tropical Western Pacific  
787 (TWP) Sites. *Meteorological Monographs*. [https://doi.org/10.1175/amsmonographs-](https://doi.org/10.1175/amsmonographs-d-15-0024.1)  
788 [d-15-0024.1](https://doi.org/10.1175/amsmonographs-d-15-0024.1)
- 789 Matus, A. V., & L'Ecuyer, T. S. (2017). The role of cloud phase in Earth's radiation budget.  
790 *Journal of Geophysical Research*. <https://doi.org/10.1002/2016JD025951>
- 791 Matus, A. V., L'Ecuyer, T. S., & Henderson, D. S. (2019). New Estimates of Aerosol  
792 Direct Radiative Effects and Forcing From A-Train Satellite Observations.  
793 *Geophysical Research Letters*. <https://doi.org/10.1029/2019GL083656>
- 794 Minnis, P., Sun-Mack, S., Young, D. F., Heck, P. W., Garber, D. P., Chen, Y., ... Yang, P.  
795 (2011). CERES edition-2 cloud property retrievals using TRMM VIRS and Terra and  
796 Aqua MODIS data-Part I: Algorithms. *IEEE Transactions on Geoscience and Remote*  
797 *Sensing*. <https://doi.org/10.1109/TGRS.2011.2144601>
- 798 Pendergrass, A. G., Conley, A., & Vitt, F. M. (2018). Surface and top-of-Atmosphere  
799 radiative feedback kernels for cesm-cam5. *Earth System Science Data*.  
800 <https://doi.org/10.5194/essd-10-317-2018>
- 801 Previdi, M. (2010). Radiative feedbacks on global precipitation. *Environmental Research*  
802 *Letters*. <https://doi.org/10.1088/1748-9326/5/2/025211>
- 803 Riihimaki, L. D., Gaustad, K., & McFarlane, S. A. (2012). Climate Science for a  
804 Sustainable Energy Future Atmospheric Radiation Measurement Best Estimate  
805 (CSSEFARMBE), PNNL-21831, 28 pp., Pac. Northwest Natl. Lab., Richland, Wash.  
806 Available at [http://www.pnnl.gov/](http://www.pnnl.gov/main/publications/external/technical_reports/PNNL-21831.pdf)  
807 [main/publications/external/technical\\_reports/PNNL-21831.pdf](http://www.pnnl.gov/main/publications/external/technical_reports/PNNL-21831.pdf).

808 Sanderson, B. M., & Shell, K. M. (2012). Model-specific radiative kernels for calculating  
809 cloud and noncloud climate feedbacks. *Journal of Climate*.  
810 <https://doi.org/10.1175/JCLI-D-11-00726.1>

811 Shell, K. M., Kiehl, J. T., & Shields, C. A. (2008). Using the radiative kernel technique to  
812 calculate climate feedbacks in NCAR's Community Atmospheric Model. *Journal of*  
813 *Climate*. <https://doi.org/10.1175/2007JCLI2044.1>

814 Sisterson, D. L., Peppler, R. A., Cress, T. S., Lamb, P. J., & Turner, D. D. (2016). The  
815 ARM Southern Great Plains (SGP) Site. *Meteorological Monographs*.  
816 <https://doi.org/10.1175/amsmonographs-d-16-0004.1>

817 Sledd, A., & L'Ecuyer, T. (2019). How much do clouds mask the impacts of arctic sea  
818 ice and snow cover variations? Different perspectives from observations and  
819 reanalyses. *Atmosphere*. <https://doi.org/10.3390/atmos10010012>

820 Sledd, A., & L'Ecuyer, T. (2020). Uncertainty in Forced and Natural Arctic Solar  
821 Absorption Variations in CMIP6 Models. *Journal of Climate*.  
822 <https://doi.org/10.1175/jcli-d-20-0244.1>

823 Soden, B. J., & Held, I. M. (2006). An assessment of climate feedbacks in coupled ocean-  
824 atmosphere models. *Journal of Climate*. <https://doi.org/10.1175/JCLI3799.1>

825 Soden, B. J., Held, I. M., Colman, R. C., Shell, K. M., Kiehl, J. T., & Shields, C. A. (2008).  
826 Quantifying climate feedbacks using radiative kernels. *Journal of Climate*.  
827 <https://doi.org/10.1175/2007JCLI2110.1>

828 Stoffel, T. (2005), Solar Infrared Radiation Station (SIRS) Handbook, *Tech. Rep., ARM*  
829 *TR-025*, 29 pp., Atmos. Radiat. Measure. Program, U. S. Dep. of Energy, Washington,  
830 D. C.

831 Stokes, G. M., & Schwartz, S. E. (1994). The Atmospheric Radiation Measurement (ARM)  
832 Program: programmatic background and design of the cloud and radiation test bed.  
833 *Bulletin - American Meteorological Society*. [https://doi.org/10.1175/1520-](https://doi.org/10.1175/1520-0477(1994)075<1201:TARMPP>2.0.CO;2)  
834 [0477\(1994\)075<1201:TARMPP>2.0.CO;2](https://doi.org/10.1175/1520-0477(1994)075<1201:TARMPP>2.0.CO;2)

835 Stokes, G. M., (2016). Original ARM concept and launch. *The Atmospheric Radiation*  
836 *Measurement (ARM) Program: The First 20 Years*, Meteor. Monogr., No. 57, Amer.  
837 Meteor. Soc., doi:10.1175/AMSMONOGRAPHS-D-15-0021.1.

838 Verlinde, J., Zak, B. D., Shupe, M. D., Ivey, M. D., & Stamnes, K. (2016). The ARM North  
839 Slope of Alaska (NSA) Sites. *Meteorological Monographs*.  
840 <https://doi.org/10.1175/amsmonographs-d-15-0023.1>

- Vial, J., Dufresne, J. L., & Bony, S. (2013). On the interpretation of inter-model spread in CMIP5 climate sensitivity estimates. *Climate Dynamics*.  
<https://doi.org/10.1007/s00382-013-1725-9>
- Wielicki, B. A., Barkstrom, B. R., Harrison, E. F., Lee, R. B., Smith, G. L., & Cooper, J. E. (1996). Clouds and the Earth's Radiant Energy System (CERES): An Earth Observing System Experiment. *Bulletin of the American Meteorological Society*.  
[https://doi.org/10.1175/1520-0477\(1996\)077<0853:CATERE>2.0.CO;2](https://doi.org/10.1175/1520-0477(1996)077<0853:CATERE>2.0.CO;2)
- Xie, S., McCoy, R. B., Klein, S. A., Cederwall, R. T., Wiscombe, W. J., Jensen, M. P., ... Turner, D. D. (2010). CLOUDS AND MORE: ARM Climate Modeling Best Estimate Data. *Bulletin of the American Meteorological Society*.  
<https://doi.org/10.1175/2009bams2891.1>
- Zelinka, M. D., Klein, S. A., & Hartmann, D. L. (2012a). Computing and partitioning cloud feedbacks using cloud property histograms. Part I: Cloud radiative kernels. *Journal of Climate*. <https://doi.org/10.1175/JCLI-D-11-00248.1>
- Zelinka, M. D., Klein, S. A., & Hartmann, D. L. (2012b). Computing and partitioning cloud feedbacks using cloud property histograms. Part II: Attribution to changes in cloud amount, altitude, and optical depth. *Journal of Climate*, 25(11), 3736–3754. <https://doi.org/10.1175/JCLI-D-11-00249.1>
- Zelinka, M. D., Myers, T. A., McCoy, D. T., Po-Chedley, S., Caldwell, P. M., Ceppi, P., ... Taylor, K. E. (2020). Causes of Higher Climate Sensitivity in CMIP6 Models. *Geophysical Research Letters*. <https://doi.org/10.1029/2019GL085782>

Abs Bias RMSE RMSE* Corr	SW SFC	SW TOA	SW ATM	LW SFC	LW TOA	LW ATM
SGP C1	0.93 (31%)	0.48 (4%)	0.68 (89%)	1.94 (-8%)	0.63 (21%)	1.81 (-16%)
	1.29 (43%)	0.61 (5%)	0.98 (113%)	2.59 (-8%)	0.79 (27%)	2.35 (-11%)
	<b>0.09</b>	<b>0.05</b>	<b>0.45</b>	<b>0.28</b>	<b>0.09</b>	<b>0.20</b>
	1.00	1.00	0.92	0.98	1.00	0.98
NSA C1	1.10 (3%)	0.88 (19%)	1.22 (21%)	7.34 (8%)	2.12 (22%)	8.71 (15%)
	1.76 (-4%)	1.36 (13%)	1.80 (29%)	8.71 (8%)	2.67 (28%)	10.40 (16%)
	<b>0.17</b>	<b>0.14</b>	<b>1.49</b>	<b>1.10</b>	<b>0.61</b>	<b>1.04</b>
	0.99	0.99	0.59	0.66	0.81	0.67
TWP C1	0.56 (40%)	0.21 (40%)	0.42 (45%)	0.76 (10%)	0.60 (100%)	0.61 (-31%)
	0.70 (46%)	0.27 (59%)	0.52 (44%)	0.89 (9%)	0.86 (126%)	0.78 (-27%)
	<b>0.04</b>	<b>0.02</b>	<b>0.38</b>	<b>0.23</b>	<b>0.05</b>	<b>0.06</b>
	1.00	1.00	0.98	0.99	1.00	1.00
TWP C2	0.72 (-5%)	0.15 (50%)	0.76 (-6%)	2.27 (18%)	2.40 (-18%)	1.62 (-13%)
	0.96 (2%)	0.18 (38%)	1.01 (3%)	3.16 (32%)	3.49 (-3%)	2.22 (-20%)
	<b>0.04</b>	<b>0.01</b>	<b>0.42</b>	<b>0.35</b>	<b>0.15</b>	<b>0.14</b>
	1.00	1.00	0.93	0.96	0.99	0.99
TWP C3	0.69 (38%)	0.25 (79%)	0.69 (44%)	2.24 (54%)	1.32 (116%)	1.63 (47%)
	0.92 (59%)	0.33 (83%)	0.87 (53%)	2.72 (63%)	1.67 (129%)	2.17 (68%)
	<b>0.05</b>	<b>0.02</b>	<b>0.35</b>	<b>0.29</b>	<b>0.10</b>	<b>0.13</b>
	1.00	1.00	0.98	0.99	1.00	0.99
ENA C1	0.43	0.35	0.30	1.18	0.57	1.12
	0.54	0.45	0.37	1.47	0.69	1.38
	<b>0.07</b>	<b>0.06</b>	<b>0.35</b>	<b>0.37</b>	<b>0.14</b>	<b>0.22</b>
	1.00	1.00	0.95	0.95	0.99	0.98

Table 1. Statistics of the comparison between monthly anomalies of **total-sky** shortwave (SW) and longwave (LW) fluxes extracted from **ERA5** and monthly kernel-estimated changes in **total-sky** SW and LW fluxes at surface (SFC), top-of-atmosphere (TOA), and in the atmospheric column (ATM; which represents TOA minus SFC) for the six ARM sites: SGP C1, NSA C1, TWP C1, TWP C2, TWP C3, and ENA C1 during the periods shown in Fig. 1. The kernel-estimated changes in fluxes are calculated using **ERA5** state variables. The numbers in each cell from top to bottom stand for: mean absolute bias (Abs Bias; unit: W/m<sup>2</sup>), root mean square error (RMSE; unit: W/m<sup>2</sup>), RMSE normalized by standard deviation of monthly anomalies of fluxes from ERA5 (RMSE\*; in bold), and correlation coefficient (Corr; in shade). All the correlation coefficients pass a significance level of 99%. The percentage in the parentheses for Abs Bias or RMSE represents the percentage error from the Abs Bias or RMSE for Year 2009 only. The percentage errors are not shown for the ENA C1 site due to the fact that this site does not have any data during 2009.

Abs Bias RMSE RMSE* Corr	SW SFC	SW TOA	SW ATM	LW SFC	LW TOA	LW ATM
SGP C1	3.35	0.98	3.62	5.24	1.39	5.13
	5.03	1.24	5.28	8.02	1.75	8.01
	<b>0.34 (278%)</b>	<b>0.11 (120%)</b>	<b>0.81 (80%)</b>	<b>0.76 (171%)</b>	<b>0.20 (122%)</b>	<b>0.67 (235%)</b>
	0.94	1.00	0.63	0.72	0.98	0.79
NSA C1	2.72	2.00	3.15	3.80	1.47	4.31
	4.51	3.29	5.26	4.81	2.02	5.66
	<b>0.77 (353%)</b>	<b>0.19 (36%)</b>	<b>0.33 (-78%)</b>	<b>0.50 (-55%)</b>	<b>0.54 (-11%)</b>	<b>0.52 (-50%)</b>
	0.90	0.99	0.94	0.89	0.87	0.89
TWP C1	2.97	0.77	3.16	3.45	2.97	5.49
	4.08	0.97	4.31	5.33	4.82	9.38
	<b>0.13 (225%)</b>	<b>0.04 (100%)</b>	<b>0.24 (-37%)</b>	<b>1.32 (474%)</b>	<b>0.33 (560%)</b>	<b>0.77 (1183%)</b>
	0.99	1.00	0.98	0.55	0.96	0.80
TWP C2	6.70	0.54	6.85	4.49	4.04	6.78
	9.19	0.75	9.49	6.39	6.33	11.28
	<b>0.27 (575%)</b>	<b>0.02 (100%)</b>	<b>0.61 (45%)</b>	<b>0.74 (111%)</b>	<b>0.28 (87%)</b>	<b>0.76 (443%)</b>
	0.97	1.00	0.87	0.85	0.97	0.82
TWP C3	4.28	1.00	4.43	3.81	3.17	3.75
	5.72	1.20	5.83	5.11	4.02	4.94
	<b>0.23 (360%)</b>	<b>0.09 (350%)</b>	<b>0.36 (3%)</b>	<b>0.57 (97%)</b>	<b>0.24 (140%)</b>	<b>0.31 (138%)</b>
	0.98	1.00	0.95	0.91	0.99	0.95
ENA C1	1.15	0.78	1.43	3.44	1.16	4.05
	1.48	0.94	1.73	4.35	1.45	5.14
	<b>0.19 (171%)</b>	<b>0.11 (83%)</b>	<b>0.22 (-37%)</b>	<b>0.90 (143%)</b>	<b>0.30 (114%)</b>	<b>0.80 (264%)</b>
	0.98	0.99	0.98	0.72	0.96	0.73

Table 2. Statistics of the comparison between monthly anomalies of **total-sky** SW and LW fluxes extracted from **ARM (for SFC)/CERES (for TOA)** and monthly kernel-estimated changes in **total-sky** SW and LW fluxes at SFC, TOA, and in ATM for the six ARM sites during the periods shown in Fig. 2. The kernel-estimated changes in fluxes are calculated using **ARM-observed** state variables. The four numbers in each cell from top to bottom stand for: mean absolute bias (Abs Bias; unit: W/m<sup>2</sup>), RMSE (unit: W/m<sup>2</sup>), RMSE normalized by standard deviation of monthly anomalies of fluxes from ARM/CERES (RMSE\*; in bold), and correlation coefficient (Corr; in shade). All the correlation coefficients pass a significance level of 99%, except for SFC and ATM SW fluxes at NSA C1. The percentage in the parentheses for RMSE\* represents the percentage error from ERA5 RMSE\* in Table 1.



Standard Deviation	Kernel Decomp	SGP C1	NSA C1	TWP C1	TWP C2	TWP C3	ENA C1
SW SFC	$\delta R$	14.41	5.88	31.02	33.88	25.12	7.77
	$K_\omega$	0.86	0.49	0.72	1.86	1.59	0.58
	$K_\alpha$	3.65	7.47	1.00	3.40	2.21	2.96
	$K_C$	14.57	5.13	30.91	31.69	25.80	6.97
SW TOA	$\delta R$	11.78	17.50	22.28	35.58	13.33	8.35
	$K_\omega$	0.41	0.47	0.36	0.53	0.53	0.17
	$K_\alpha$	2.39	11.99	0.12	0.04	0.71	0.13
	$K_C$	11.49	5.55	22.09	35.88	13.13	8.40
LW SFC	$\delta R$	10.58	9.53	4.03	8.59	9.03	4.82
	$K_\omega$	3.91	1.44	1.93	5.36	7.33	2.05
	$K_{T_a}$	2.73	3.91	3.14	3.12	0.76	1.22
	$K_{T_s}$	5.13	4.11	1.24	1.84	3.73	3.15
	$K_C$	7.20	6.31	4.18	6.67	4.23	4.64
LW TOA	$\delta R$	8.81	3.71	14.46	22.50	16.95	4.79
	$K_\omega$	1.87	1.00	1.84	5.26	5.28	1.16
	$K_{T_a}$	2.20	3.34	3.72	5.39	1.20	1.69
	$K_{T_s}$	1.53	1.02	0.08	0.24	0.98	0.75
	$K_C$	6.59	2.56	13.47	19.11	14.37	4.23

Table 3. Standard deviation of monthly anomalies of **total-sky** SW and LW fluxes directly from **ARM (for SFC)/CERES (for TOA)** ( $\delta R$ , in shade) and each kernel-estimated responses of **total-sky** SW and LW fluxes calculated using the corresponding **ARM-observed** state variable at SFC and TOA for the six ARM sites during the periods shown in Fig. 2. The SW kernel-estimated responses at SFC and TOA are decomposed into water vapor ( $K_\omega$ ), surface albedo ( $K_\alpha$ ), and cloud ( $K_C$ ) kernel-estimated responses. The LW kernel-estimated responses at SFC and TOA are decomposed into water vapor ( $K_\omega$ ), air temperature ( $K_{T_a}$ ), surface temperature ( $K_{T_s}$ ) and cloud ( $K_C$ ) kernel-estimated responses.

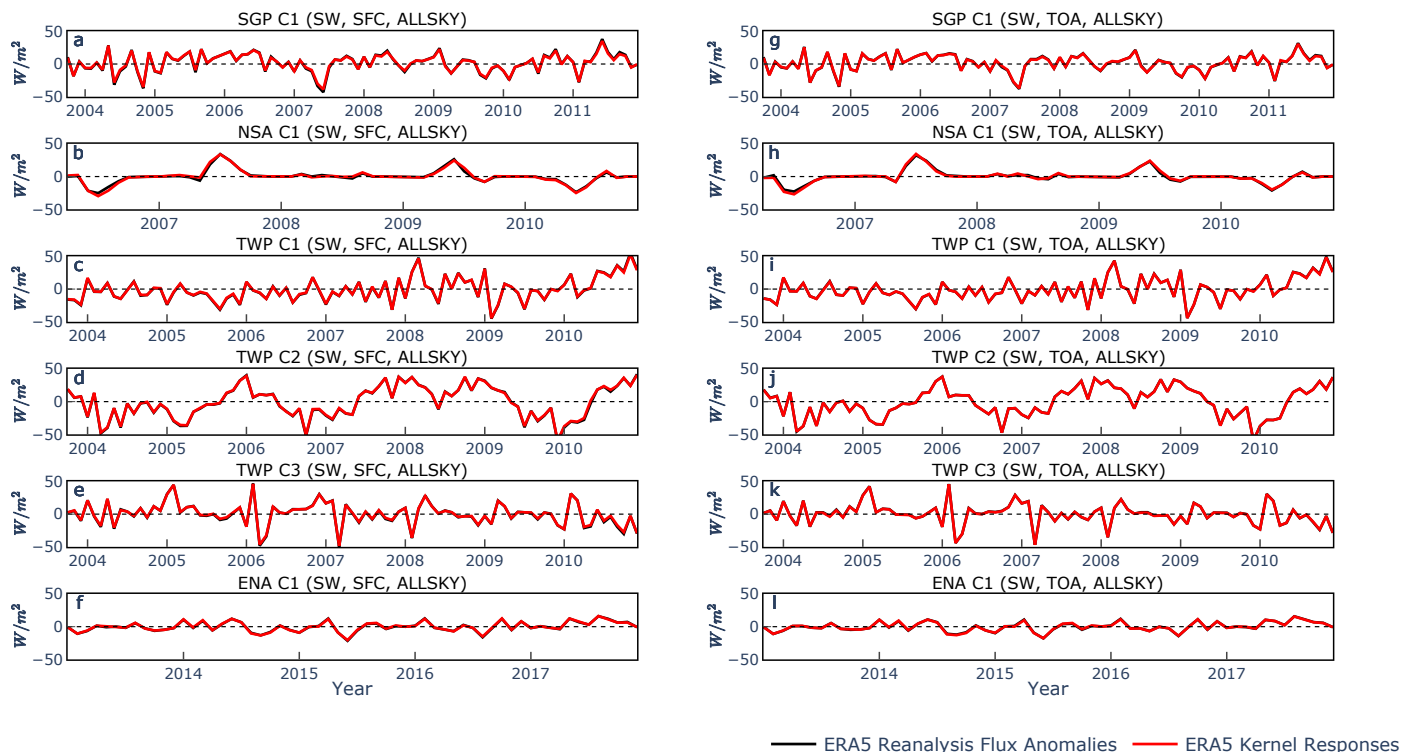


Figure 1. A comparison of the time series of monthly kernel-estimated changes in total-sky SW fluxes (red) with monthly anomalies of total-sky SW fluxes extracted from **ERA5** (black) at surface (SFC; a-f) and top-of-atmosphere (TOA; g-l) for the six ARM sites: SGP C1, NSA C1, TWP C1, TWP C2, TWP C3, and ENA C1. The kernel-estimated responses are calculated using **ERA5** water vapor and surface albedo.

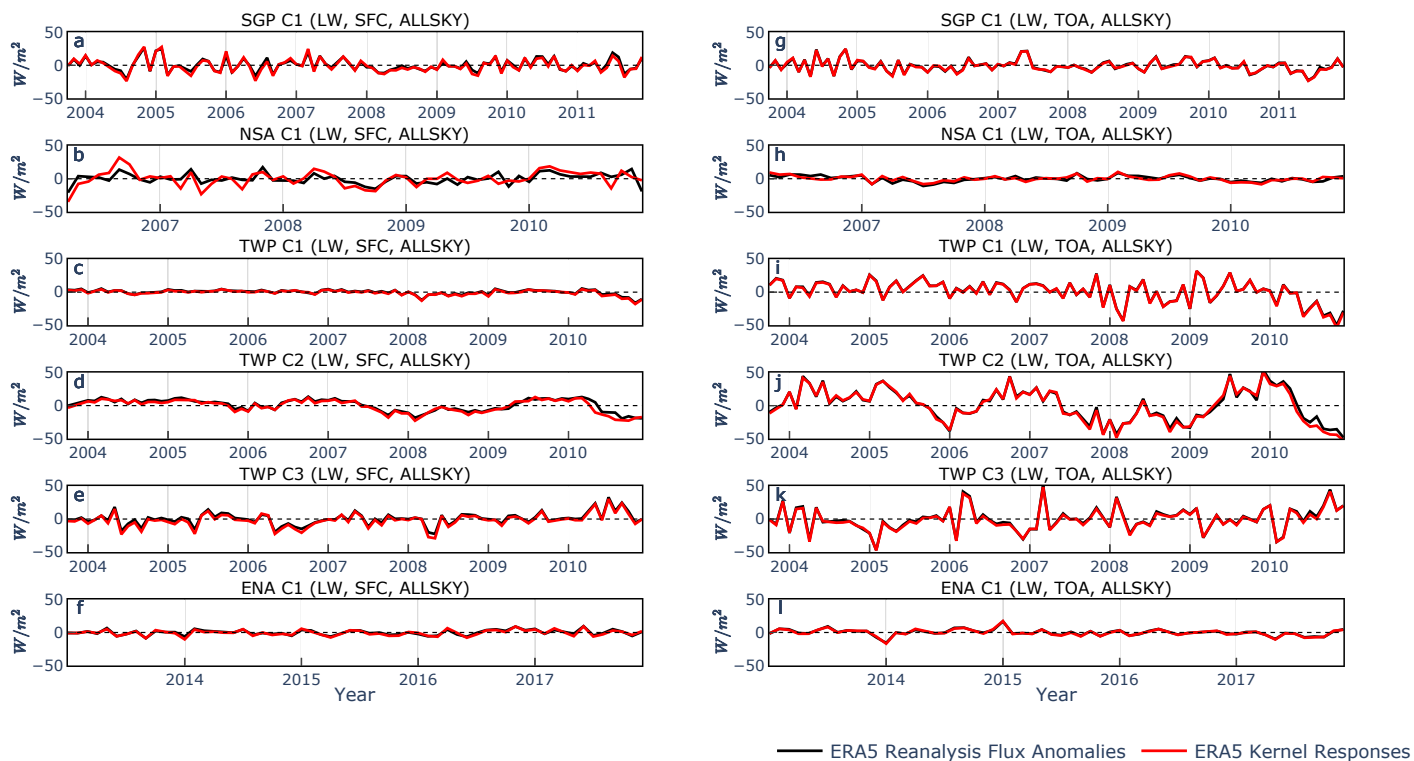


Figure 2. Same as Figure 1, but for monthly kernel-estimated changes in total-sky LW fluxes (red) and monthly anomalies of total-sky LW fluxes extracted from **ERA5** (black). The kernel-estimated responses are calculated using **ERA5** water vapor and air and surface temperature.

### ERA5 reanalysis flux anomalies VS ERA5 kernel responses (ALLSKY)

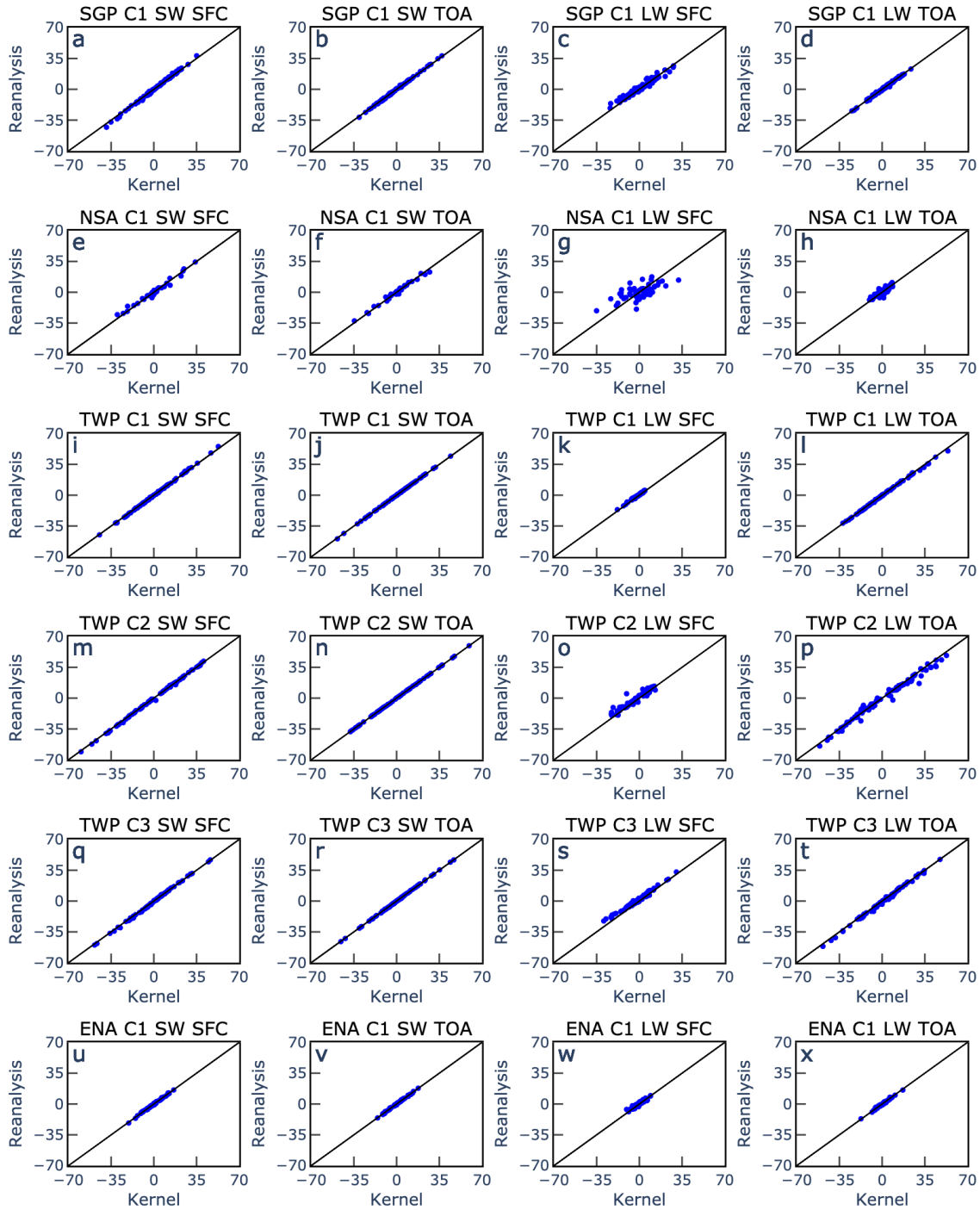


Figure 3. Scatter plots for monthly anomalies of total-sky SW and LW fluxes from **ERA5** versus monthly kernel-estimated changes in total-sky SW and LW fluxes at SFC and TOA calculated using the **ERA5** state variables for the six ARM sites.

# ARM/CERES flux anomalies VS ARM kernel responses (ALLSKY)

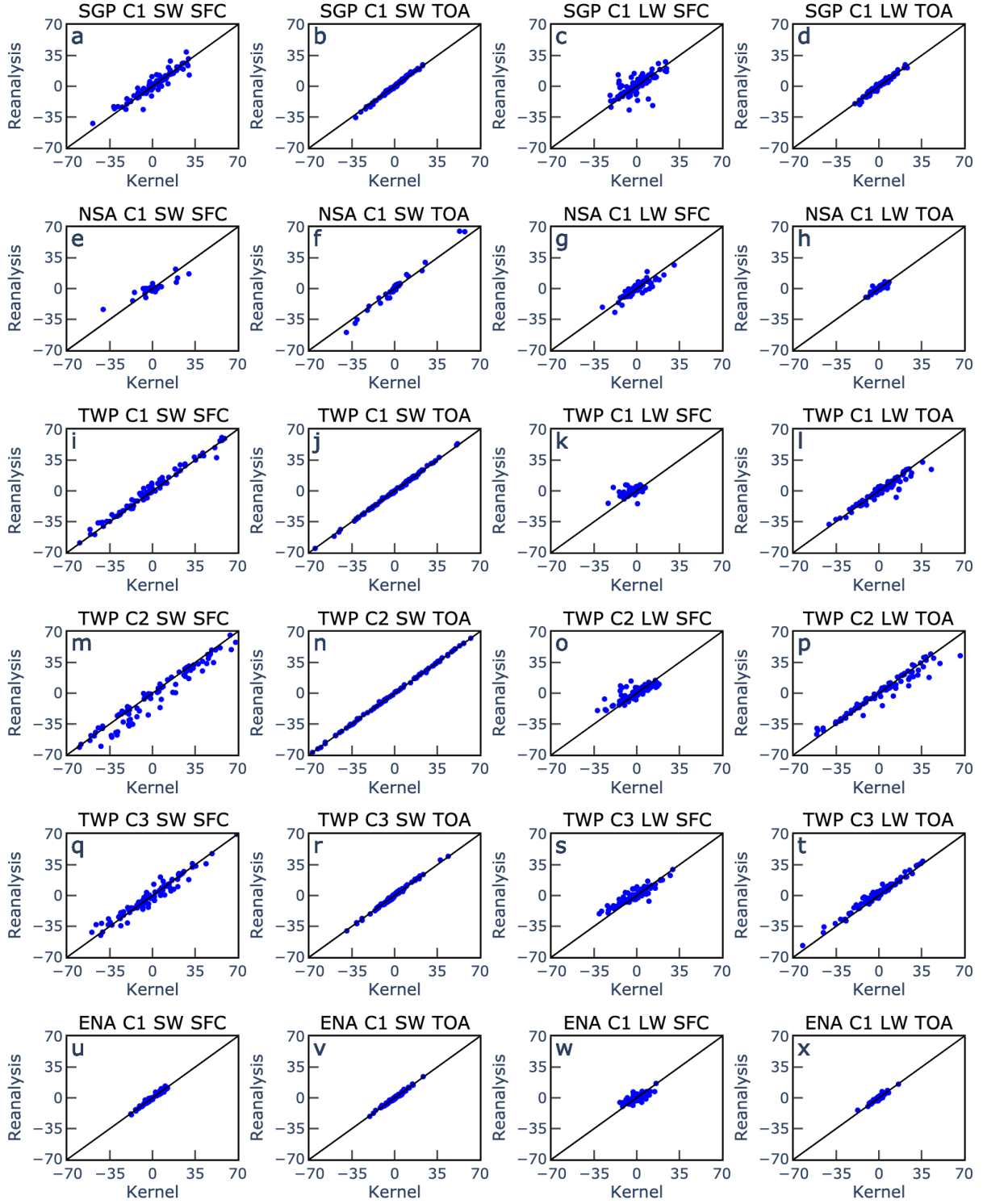


Figure 4. Scatter plots for monthly anomalies of observed total-sky SW and LW fluxes from **ARM (SFC) and CERES (TOA)** versus monthly kernel-estimated changes in total-sky SW and LW fluxes calculated using the **ARM** state variables at SFC and TOA for the six ARM sites.

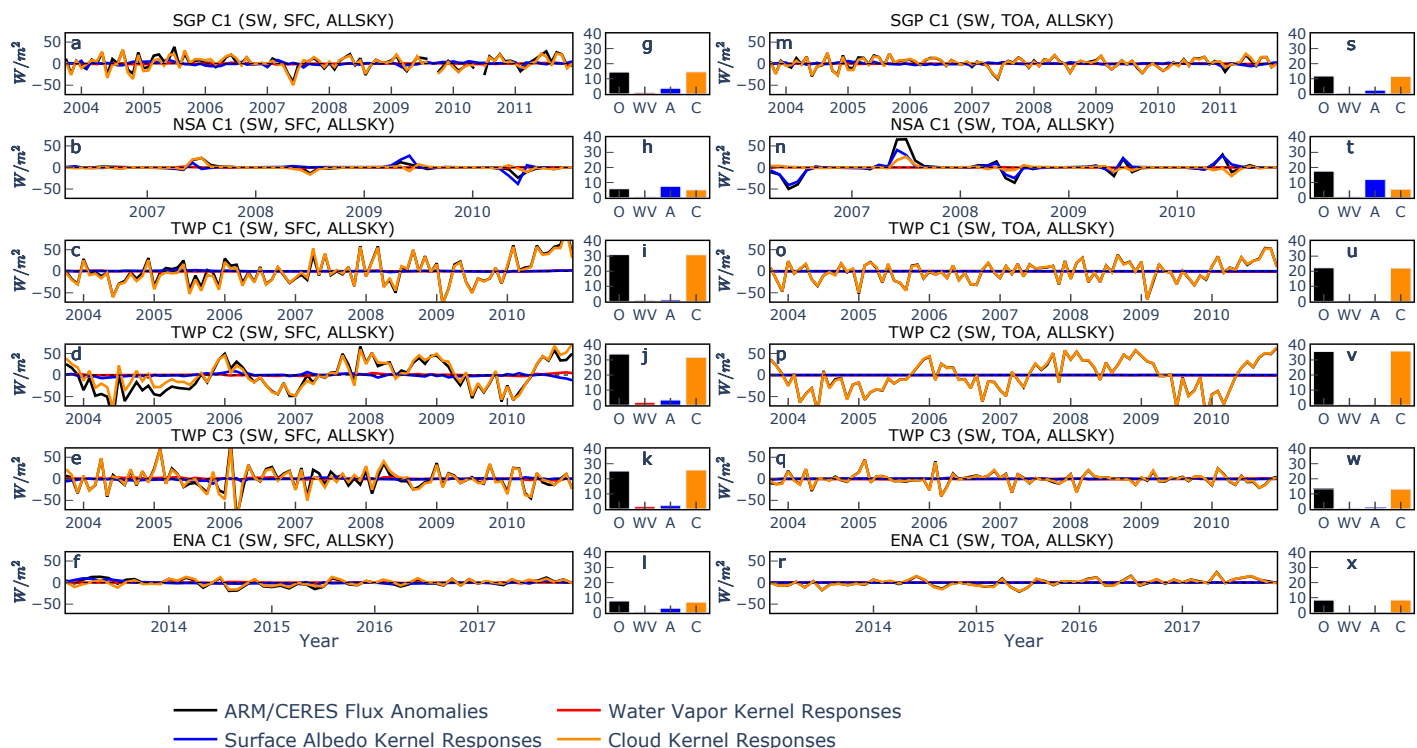


Figure 5. Decomposition of monthly kernel-estimated changes in **ARM** total-sky SW fluxes at SFC (a-f) and TOA (m-r) into SW water vapor (red), surface albedo (blue), and cloud (orange) kernel-estimated changes for the six ARM sites. These kernel-estimated responses are calculated using **ARM-observed** water vapor and surface albedo. Black line represents monthly anomalies of observed total-sky SW fluxes from ARM (for SFC) and CERES (for TOA). g-l, bar charts of standard deviation of lines in a-f. s-x, bar charts of standard deviation of lines in m-r. Black bar (O) stands for standard deviation of observed total-sky SW flux anomalies from ARM or CERES, red for water vapor kernel-estimated changes in SW fluxes, blue for surface albedo kernel-estimated changes, and orange for cloud kernel-estimated changes.

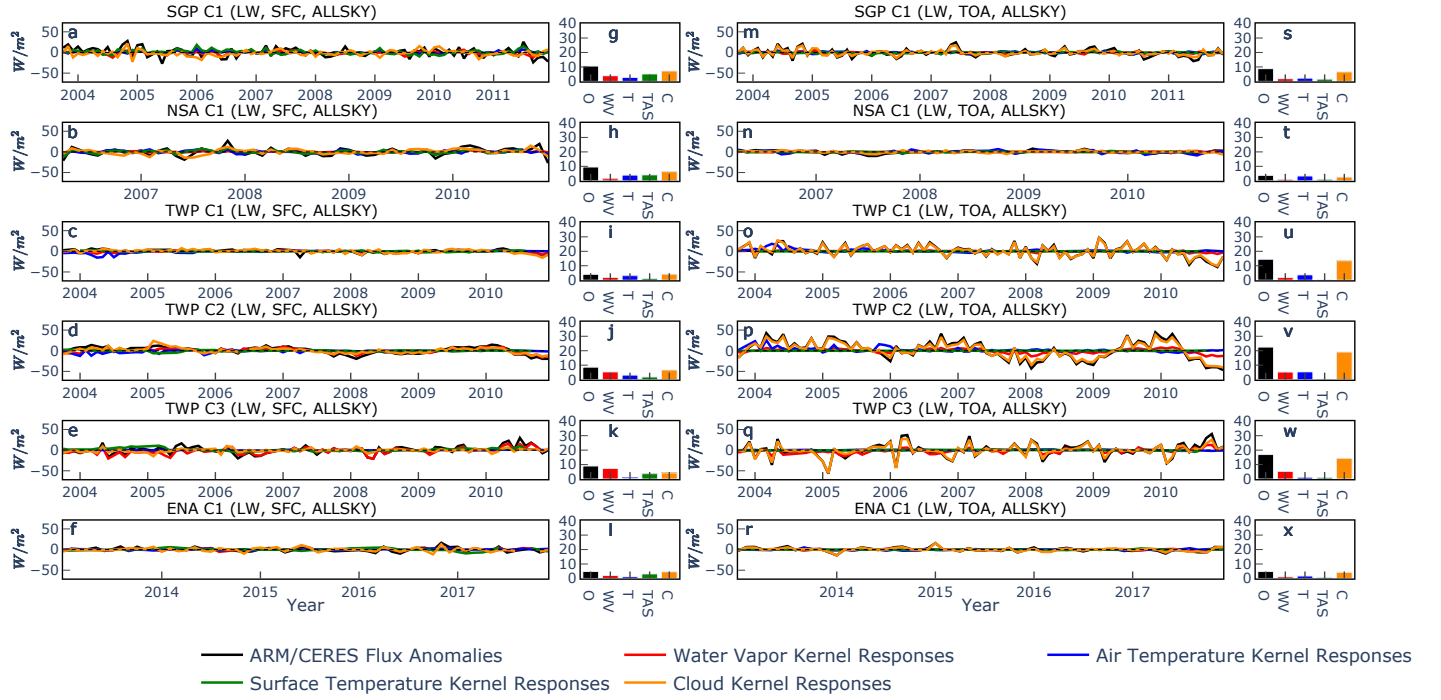


Figure 6. Decomposition of monthly kernel-estimated changes in **ARM** total-sky LW fluxes at SFC (a-f) and TOA (m-r) into LW water vapor (red), air temperature (blue), surface temperature (green), and cloud (orange) kernel-estimated changes for the six ARM sites. These kernel-estimated responses are calculated using **ARM-observed** water vapor and air and surface temperature. Black line represents monthly anomalies of observed total-sky LW fluxes from ARM (for SFC) and CERES (for TOA). g-l, bar charts of standard deviation of lines in a-f. s-x, bar charts of standard deviation of lines in m-r. Black bar (O) stands for standard deviation of observed total-sky LW flux anomalies from ARM or CERES, red for water vapor kernel-estimated changes in LW fluxes, blue for surface albedo kernel-estimated changes, and orange for cloud kernel-estimated changes.

Vertical profiles of WV or T kernel responses in ERA5 and ARM

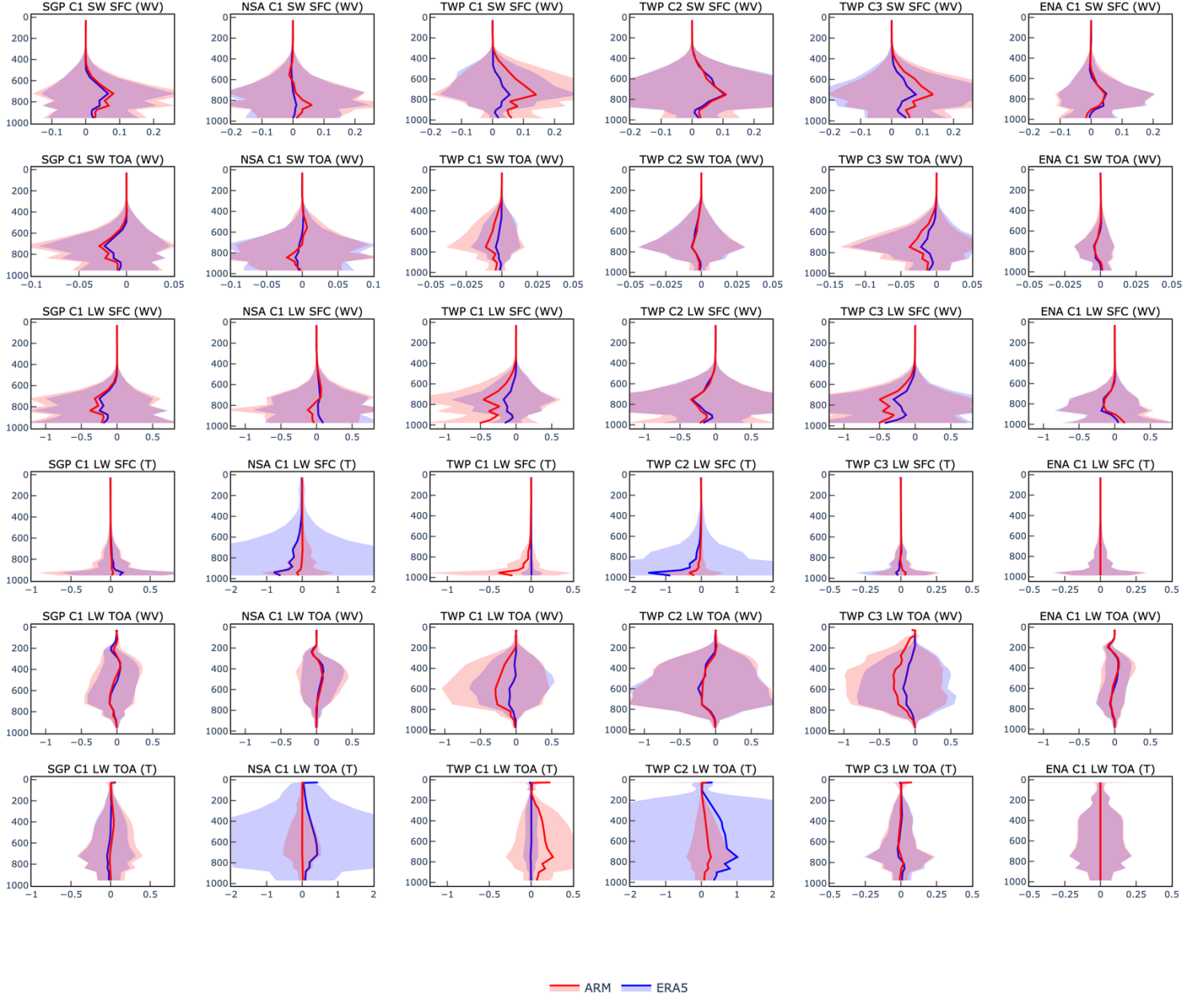


Figure 7. Comparison of vertical profiles of water vapor (WV) and temperature (T) kernel-estimated changes in clear-sky SW and LW fluxes (unit:  $\text{W/m}^2$ ) calculated using ARM (red) and ERA5 (blue) state variables at SFC and TOA for the six ARM sites. The red and blue lines are the average of water vapor or temperature kernel responses over the chosen period in Fig. 1; the red and blue shades represent the standard deviation of the kernel responses during the period.



*Journal of Geophysical Research: Atmosphere*

Supporting Information for

**Evaluation of CloudSat Radiative Kernels Using ARM and CERES Observations  
and ERA5 Reanalysis**

Ni Dai<sup>1\*</sup>, Ryan J. Kramer<sup>2,3</sup>, Brian J. Soden<sup>4</sup>, and Tristan S. L'Ecuyer<sup>5</sup>

<sup>1</sup>*Joint Institute for Regional Earth System Science & Engineering, University of  
California, Los Angeles, Los Angeles, CA, 90095, USA*

<sup>2</sup>*Climate and Radiation Laboratory, Earth Sciences Division, NASA Goddard Space  
Flight Center, Greenbelt, MD, 20771, USA*

<sup>3</sup>*Joint Center for Earth Systems Technology, University of Maryland at Baltimore  
County, Baltimore, MD, USA*

<sup>4</sup>*Rosenstiel School of Marine and Atmospheric Sciences, University of Miami, Miami, FL,  
33149, USA*

<sup>5</sup>*Department of Atmospheric and Oceanic Sciences, University of Wisconsin-Madison,  
Madison, WI, 53706, USA*

Corresponding Author: Ni Dai (ndai@umd.edu)

**Contents of this file**

Figures S1 to S9 and Table S1 to S6

905

a. Total number of hours with valid values of air temperature

	6hr	12hr	18hr	24hr
SGP C1 ( <b>0.47%</b> )	3003	2970	2981	3018
NSA C1 ( <b>4.09%</b> )	1440		1222	1283
TWP C1 ( <b>0.98%</b> )		2428		2525
TWP C2 ( <b>2.43%</b> )		1959		2159
TWP C3 ( <b>0.43%</b> )		2677		2723
ENA C1 ( <b>0.39%</b> )		1790		1762

906

907

b. Total number of hours with valid values of relative humidity

	6hr	12hr	18hr	24hr
SGP C1 ( <b>0.44%</b> )	2994	2958	2975	3011
NSA C1 ( <b>4.11%</b> )	1435		1217	1283
TWP C1 ( <b>1.05%</b> )		2394		2497
TWP C2 ( <b>2.61%</b> )		1927		2139
TWP C3 ( <b>0.41%</b> )		2673		2717
ENA C1 ( <b>0.42%</b> )		1788		1758

908

Table S1. Total number of hours with valid values of air temperature (a) and relative humidity (b) at each selected hour (6hr, 12hr, 18hr, and 24hr) for the six ARM sites: SGP C1, NSA C1, TWP C1, TWP C2, TWP C3, and ENA C1 during the periods shown in Fig. 1. Percentages in the parentheses stand for the percentage difference between the maximum and minimum number of hours at each site.

913

914

915

916

917

918

919

920

921

922

923

924

925

926

927

928

929

930

931

932

933

934

935

936

937

Abs Bias RMSE Correlation	SW SFC	SW TOA	SW ATM	LW SFC	LW TOA	LW ATM
SGP C1	0.93 (29%)	0.48 (4%)	0.68 (89%)	1.94 (-8%)	0.63 (21%)	1.81 (-16%)
	1.29 (43%)	0.61 (5%)	0.98 (113%)	2.59 (-8%)	0.79 (27%)	2.35 (-11%)
	<b>0.31</b>	<b>0.17</b>	<b>0.50</b>	<b>0.29</b>	<b>0.18</b>	<b>0.20</b>
	0.95	0.99	0.89	0.98	0.99	0.99
NSA C1	1.10 (2%)	0.88 (19%)	1.23 (23%)	7.34 (8%)	2.12 (23%)	8.71 (15%)
	1.76 (-4%)	1.36 (13%)	1.80 (29%)	8.71 (8%)	2.67 (28%)	10.40 (13%)
	<b>0.18</b>	<b>0.15</b>	<b>1.34</b>	<b>1.31</b>	<b>0.82</b>	<b>1.11</b>
	0.99	1.00	0.58	0.53	0.72	0.63
TWP C1	0.56 (40%)	0.21 (40%)	0.42 (45%)	0.76 (10%)	0.60 (100%)	0.61 (-30%)
	0.70 (45%)	0.27 (59%)	0.52 (44%)	0.89 (9%)	0.86 (126%)	0.78 (-27%)
	<b>0.43</b>	<b>1.00</b>	<b>0.35</b>	<b>0.31</b>	<b>0.22</b>	<b>0.25</b>
	0.97	-0.42	0.99	0.98	0.99	0.97
TWP C2	0.72 (-5%)	0.15 (50%)	0.76 (-6%)	2.27 (18%)	2.40 (-18%)	1.62 (-13%)
	0.96 (2%)	0.18 (38%)	1.01 (3%)	3.16 (32%)	3.49 (-3%)	2.22 (-20%)
	<b>0.36</b>	<b>1.00</b>	<b>0.36</b>	<b>0.39</b>	<b>0.56</b>	<b>0.59</b>
	0.95	0.50	0.95	0.95	0.92	0.82
TWP C3	0.69 (38%)	0.25 (78%)	0.69 (41%)	2.24 (54%)	1.32 (103%)	1.63 (47%)
	0.92 (59%)	0.33 (83%)	0.87 (53%)	2.72 (63%)	1.67 (120%)	2.17 (111%)
	<b>0.41</b>	<b>0.94</b>	<b>0.35</b>	<b>0.33</b>	<b>0.32</b>	<b>0.29</b>
	0.98	0.75	0.98	0.99	0.97	0.97
ENA C1	0.43	0.35	0.30	1.18	0.57	1.12
	0.54	0.45	0.37	1.46	0.69	1.38
	<b>0.52</b>	<b>1.00</b>	<b>0.40</b>	<b>0.27</b>	<b>0.48</b>	<b>0.22</b>
	0.88	0.10	0.93	0.97	0.92	0.98

938

939 Table S2. Statistics of the comparison between monthly **clear-sky** SW and LW anomalies  
940 directly from **ERA5** and monthly **clear-sky** kernel-estimated changes in SW and LW  
941 fluxes at surface (SFC), top-of-atmosphere (TOA), and in the atmospheric column (ATM;  
942 which represents TOA minus SFC) for the six ARM sites: SGP C1, NSA C1, TWP C1,  
943 TWP C2, TWP C3, and ENA C1 during the periods shown in Fig. 1. The kernel-estimated  
944 responses are calculated using **ERA5** state variables. The four numbers in each cell from  
945 top to bottom stand for: mean absolute bias (unit: W/m<sup>2</sup>), root mean square error (RMSE;  
946 unit: W/m<sup>2</sup>), RMSE normalized by standard deviation of monthly clear-sky anomalies  
947 directly from ERA5 (RMSE\*; in bold), and correlation coefficient (in shade). All the  
948 correlation coefficients pass a significance level of 99%, except for the TOA SW flux at  
949 TWP C1 and ENA C1. The percentage in the parentheses for Abs Bias or RMSE represents  
950 the percentage error from the Abs Bias or RMSE for Year 2009 only. The percentage errors  
951 are not shown for the ENA C1 site due to the fact that this site does not have any data  
952 during 2009.

953

954

955

956

Standard Deviation	Kernel Decomp	SGP C1	NSA C1	TWP C1	TWP C2	TWP C3	ENA C1
SW SFC	$\delta R$	14.58	10.17	18.07	24.12	17.41	7.52
	$K_\omega$	0.87	0.92	0.69	1.94	1.48	0.59
	$K_\alpha$	2.69	6.71	0.00	0.00	0.03	0.00
	$K_C$	12.47	8.40	17.00	22.10	16.03	7.51
SW TOA	$\delta R$	12.83	9.38	17.08	22.08	15.89	7.11
	$K_\omega$	0.42	0.86	0.35	0.52	0.49	0.17
	$K_\alpha$	2.55	6.31	0.00	0.00	0.03	0.00
	$K_C$	12.09	7.81	17.23	22.41	16.10	7.11
LW SFC	$\delta R$	9.32	7.95	3.80	8.92	9.30	3.95
	$K_\omega$	3.97	2.20	1.61	5.53	6.86	1.97
	$K_{T_a}$	2.69	6.16	0.48	0.55	0.72	1.19
	$K_{T_s}$	5.24	4.18	0.76	0.94	2.00	1.90
	$K_C$	6.54	5.25	2.88	3.69	2.41	3.47
LW TOA	$\delta R$	8.88	4.38	16.68	23.79	17.47	4.86
	$K_\omega$	1.76	1.33	1.81	5.32	4.43	0.98
	$K_{T_a}$	2.49	5.47	0.82	0.83	0.85	1.45
	$K_{T_s}$	1.56	1.09	0.05	0.11	0.64	0.39
	$K_C$	6.70	3.79	15.14	20.12	14.44	4.25

Table S3. Standard deviation of monthly anomalies of **total-sky** SW and LW fluxes directly from **ERA5** ( $\delta R$ , in shade) and each kernel-estimated responses of **total-sky** SW and LW fluxes calculated using the corresponding **ERA5** state variable at SFC and TOA for the six ARM sites during the periods shown in Fig. 1. The SW kernel-estimated responses at SFC and TOA are decomposed into water vapor ( $K_\omega$ ), surface albedo ( $K_\alpha$ ), and cloud ( $K_C$ ) kernel-estimated responses. The LW kernel-estimated responses at SFC and TOA are decomposed into water vapor ( $K_\omega$ ), air temperature ( $K_{T_a}$ ), surface temperature ( $K_{T_s}$ ) and cloud ( $K_C$ ) kernel-estimated responses.

982

983

Abs Bias RMSE Correlation	SW SFC	SW TOA	SW ATM	LW SFC	LW TOA	LW ATM
SGP C1	3.35	0.98	3.62	5.24	1.39	5.13
	5.03	1.24	5.25	8.02	1.75	8.01
	<b>0.73 (135%)</b>	<b>0.37 (118%)</b>	<b>0.82 (64%)</b>	<b>0.77 (165%)</b>	<b>0.40 (122%)</b>	<b>0.64 (220%)</b>
	0.69	0.93	0.57	0.71	0.92	0.80
NSA C1	2.72	2.00	3.15	3.80	1.47	4.31
	4.51	3.29	5.26	4.81	2.02	5.66
	<b>0.60 (233%)</b>	<b>0.15 (0%)</b>	<b>0.21 (-84%)</b>	<b>0.60 (-54%)</b>	<b>0.65 (21%)</b>	<b>0.56 (-98%)</b>
	0.96	1.00	0.98	0.84	0.81	0.87
TWP C1	2.97	0.77	3.16	3.45	2.97	5.49
	4.08	0.97	4.31	5.33	4.82	9.38
	<b>0.83 (93%)</b>	<b>0.99 (1%)</b>	<b>0.87 (149%)</b>	<b>1.87 (503%)</b>	<b>1.31 (495%)</b>	<b>2.16 (764%)</b>
	0.72	0.15	0.65	0.19	0.70	0.27
TWP C2	6.70	0.54	6.85	4.49	4.04	6.78
	9.19	0.75	9.49	6.39	6.33	11.28
	<b>0.86 (138%)</b>	<b>0.99 (1%)</b>	<b>0.87 (142%)</b>	<b>1.06 (172%)</b>	<b>1.00 (79%)</b>	<b>2.55 (332%)</b>
	0.78	0.24	0.77	0.72	0.79	0.15
TWP C3	4.28	1.00	4.43	3.81	3.17	3.75
	5.72	1.20	5.83	5.11	4.02	4.94
	<b>0.86 (110%)</b>	<b>1.02 (9%)</b>	<b>0.88 (151%)</b>	<b>0.63 (91%)</b>	<b>0.76 (138%)</b>	<b>0.61 (110%)</b>
	0.55	0.45	0.48	0.87	0.88	0.84
ENA C1	1.15	0.78	1.43	3.44	1.16	4.05
	1.48	0.94	1.73	4.35	1.45	5.14
	<b>0.31 (-40%)</b>	<b>0.99 (1%)</b>	<b>0.36 (-10%)</b>	<b>0.84 (211%)</b>	<b>1.02 (113%)</b>	<b>0.90 (309%)</b>
	0.97	0.22	0.95	0.67	0.64	0.62

984

985 Table S4. Statistics of the comparison between monthly **clear-sky** SW and LW anomalies  
986 directly from **ARM (for SFC)/CERES (for TOA)** and monthly **clear-sky** kernel-  
987 estimated changes in SW and LW fluxes at SFC, TOA, and in ATM for the six ARM sites.  
988 The kernel-estimated responses are calculated using **ARM-observed** state variables. The  
989 four numbers in each cell from top to bottom stand for: mean absolute bias (unit: W/m<sup>2</sup>),  
990 RMSE (unit: W/m<sup>2</sup>), RMSE normalized by standard deviation of monthly clear-sky  
991 anomalies directly from ARM/CERES (in bold), and correlation coefficient (in shade). All  
992 the correlation coefficients pass a significance level of 99%, except for TOA SW at TWP  
993 C1, TWP C2, and ENA C1, and SFC/ATM LW fluxes at TWP C1 and C2. The percentage  
994 in the parentheses for RMSE\* represents the percentage error from ERA5 RMSE\* in Table  
995 S1.

996

997

998

999

1000

1001  
1002  
1003

Abs Bias RMSE RMSE* Corr	SW SFC	SW TOA	LW SFC	LW TOA
SGP C1	0.98	0.47	2.56	1.33
	1.32	0.60	3.22	1.64
	<b>0.32 (3%)</b>	<b>0.17 (0%)</b>	<b>0.37 (28%)</b>	<b>0.38 (111%)</b>
	0.95	0.99	0.96	0.92
NSA C1	0.78	0.79	2.82	1.40
	1.16	1.26	3.52	1.85
	<b>0.12 (-33%)</b>	<b>0.14 (-7%)</b>	<b>0.53 (-60%)</b>	<b>0.57 (-30%)</b>
	1.00	1.00	0.93	0.84
TWP C1	0.69	0.21	2.79	2.83
	0.88	0.28	4.46	4.72
	<b>0.54 (26%)</b>	<b>1.25 (25%)</b>	<b>1.58 (410%)</b>	<b>1.19 (441%)</b>
	0.88	-0.48	0.46	0.70
TWP C2	0.89	0.14	4.53	4.15
	1.09	0.18	6.75	6.46
	<b>0.41 (14%)</b>	<b>1.01 (1%)</b>	<b>0.84 (115%)</b>	<b>1.03 (84%)</b>
	0.92	0.48	0.72	0.78
TWP C3	0.91	0.32	3.23	2.92
	1.15	0.40	4.07	3.79
	<b>0.51 (42%)</b>	<b>1.16 (16%)</b>	<b>0.49 (48%)</b>	<b>0.71 (122%)</b>
	0.92	0.69	0.93	0.89
ENA C1	0.52	0.35	3.03	1.24
	0.62	0.45	4.17	1.56
	<b>0.60 (46%)</b>	<b>0.99 (5%)</b>	<b>0.76 (181%)</b>	<b>1.08 (125%)</b>
	0.81	0.11	0.71	0.58

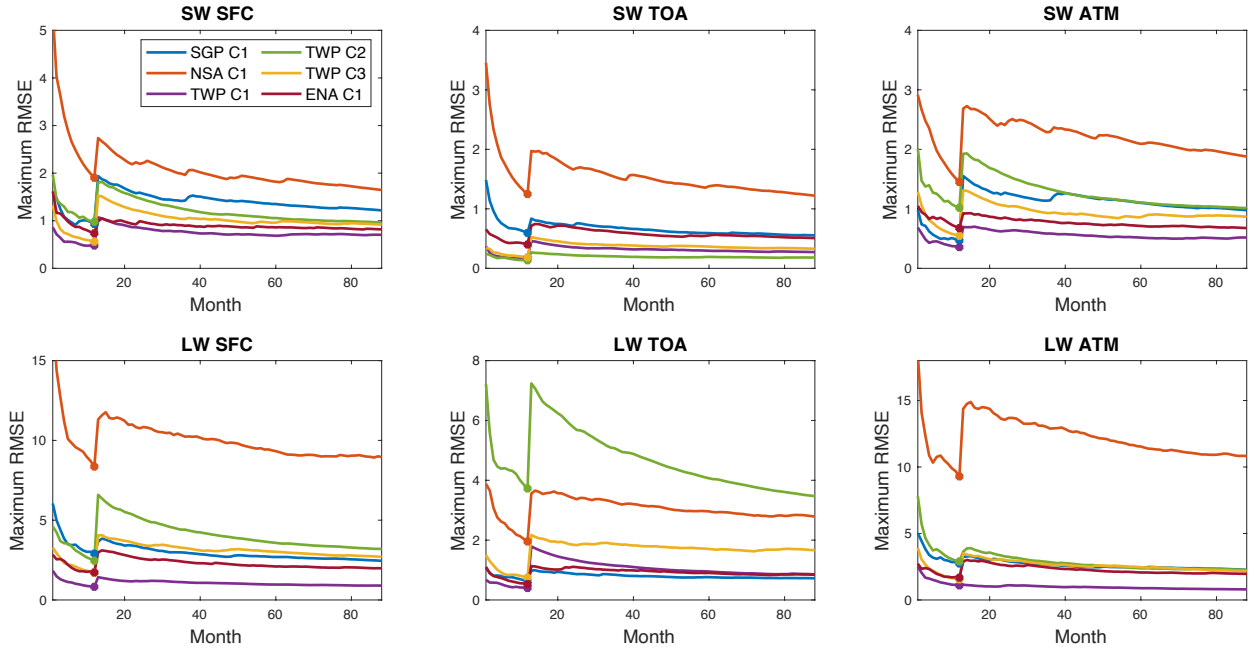
1004  
1005  
1006  
1007  
1008  
1009  
1010  
1011  
1012  
1013  
1014  
1015  
1016  
1017  
1018

Table S5. Statistics of the comparison between monthly anomalies of **clear-sky** SW and LW fluxes from **ERA5** and monthly kernel-estimated changes in **clear-sky** SW and LW fluxes at SFC, TOA, and in ATM for the six ARM sites. The kernel-estimated responses are calculated using **ARM-observed** state variables except for surface albedo, which is from ERA5 (monthly clear-sky SFC upward SW flux divided by monthly clear-sky SFC downward SW flux). The four numbers in each cell from top to bottom stand for: mean absolute bias (Abs Bias; unit: W/m<sup>2</sup>), RMSE (unit: W/m<sup>2</sup>), RMSE normalized by standard deviation of monthly clear-sky anomalies directly from ERA5 (RMSE\*; in bold), and correlation coefficient (Corr; in shade). All the correlation coefficients pass a significance level of 99%, except for TOA SW fluxes at TWP C1 and ENA C1. The percentage in the parentheses for RMSE\* represents the percentage error from ERA5 RMSE\* in Table S1.

Abs Bias RMSE RMSE* Corr	1022			
	SW SFC	SW TOA	LW SFC	LW TOA
SGP C1	3.54	0.92	5.60	0.79
	5.18	1.17	8.38	0.97
	<b>0.73 (135%)</b>	<b>0.40 (135%)</b>	<b>0.80 (176%)</b>	<b>0.22 (22%)</b>
	0.69	0.93	0.68	0.98
NSA C1	2.05	1.82	7.95	2.62
	3.32	2.87	9.23	3.20
	<b>0.30 (67%)</b>	<b>0.18 (20%)</b>	<b>1.14 (-13%)</b>	<b>1.03 (26%)</b>
	0.95	1.00	0.51	0.58
TWP C1	1.68	0.72	2.29	0.88
	2.15	0.79	3.03	1.21
	<b>0.76 (77%)</b>	<b>0.98 (2%)</b>	<b>1.08 (248%)</b>	<b>0.33 (50%)</b>
	0.68	0.20	0.51	0.98
TWP C2	4.10	0.48	3.58	2.49
	5.16	0.63	5.07	3.48
	<b>0.78 (117%)</b>	<b>1.10 (10%)</b>	<b>0.83 (113%)</b>	<b>0.56 (0%)</b>
	0.81	-0.24	0.83	0.93
TWP C3	2.83	0.79	3.55	1.65
	3.68	0.94	4.61	2.05
	<b>0.91 (122%)</b>	<b>0.96 (2%)</b>	<b>0.58 (76%)</b>	<b>0.39 (22%)</b>
	0.48	0.47	0.89	0.95
ENA C1	1.36	0.58	2.84	0.64
	1.76	0.71	3.19	0.79
	<b>0.33 (-37%)</b>	<b>1.07 (7%)</b>	<b>0.62 (130%)</b>	<b>0.56 (17%)</b>
	0.97	-0.18	0.84	0.88

Table S6. Statistics of the comparison between monthly anomalies of **clear-sky** SW and LW fluxes from **ARM (for SFC)/CERES (for TOA)** and monthly kernel-estimated changes in **clear-sky** SW and LW fluxes at SFC, TOA, and in ATM for the six ARM sites. The kernel-estimated responses are calculated using **ERA5** state variables except for surface albedo, which is from ARM/CERES surface albedo (monthly clear-sky SFC upward SW flux divided by monthly clear-sky SFC downward SW flux). The four numbers in each cell from top to bottom stand for: mean absolute bias (Abs Bias; unit: W/m<sup>2</sup>), RMSE (unit: W/m<sup>2</sup>), RMSE normalized by standard deviation of monthly clear-sky anomalies directly from ARM/CERES (RMSE\*; in bold), and correlation coefficient (Corr; in shade). All the correlation coefficients pass a significance level of 99%, except for TOA SW at TWP C1, TWP C2, and ENA C1. The percentage in the parentheses for RMSE\* represents the percentage error from ERA5 RMSE\* in Table S1.

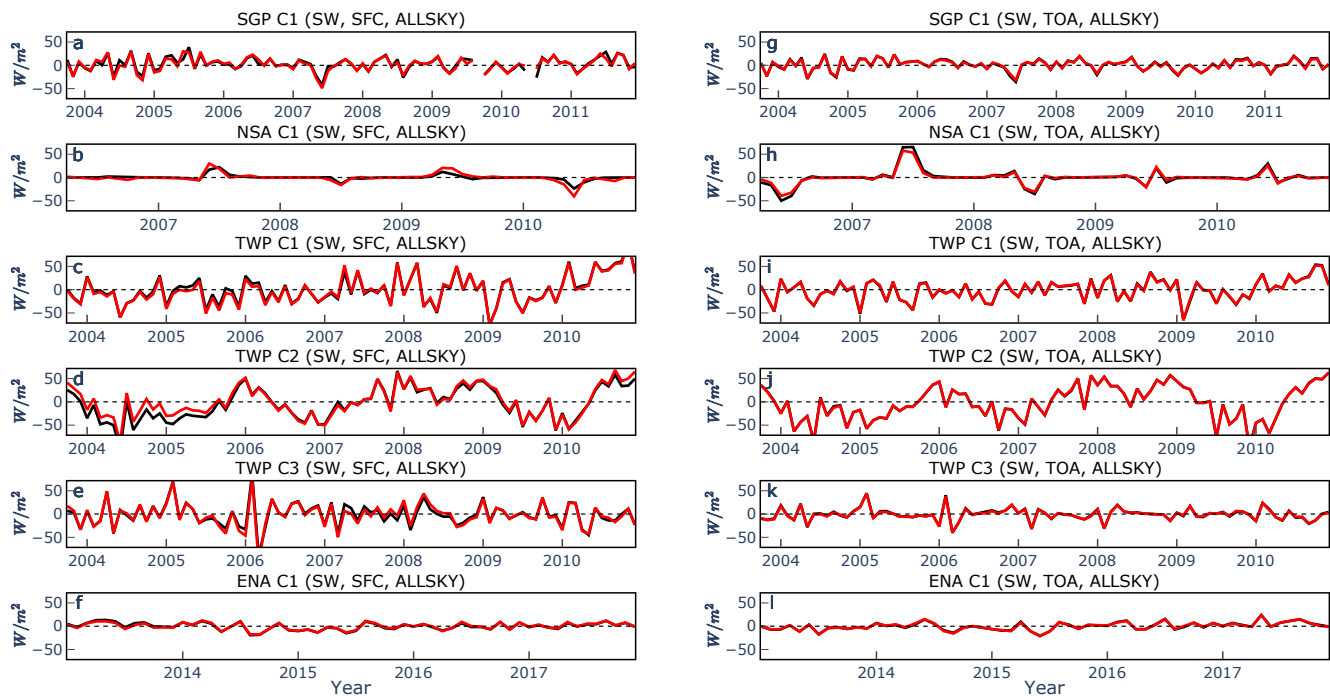
1038  
1039  
1040  
1041



1042  
1043  
1044  
1045  
1046  
1047  
1048  
1049  
1050  
1051  
1052  
1053  
1054  
1055  
1056

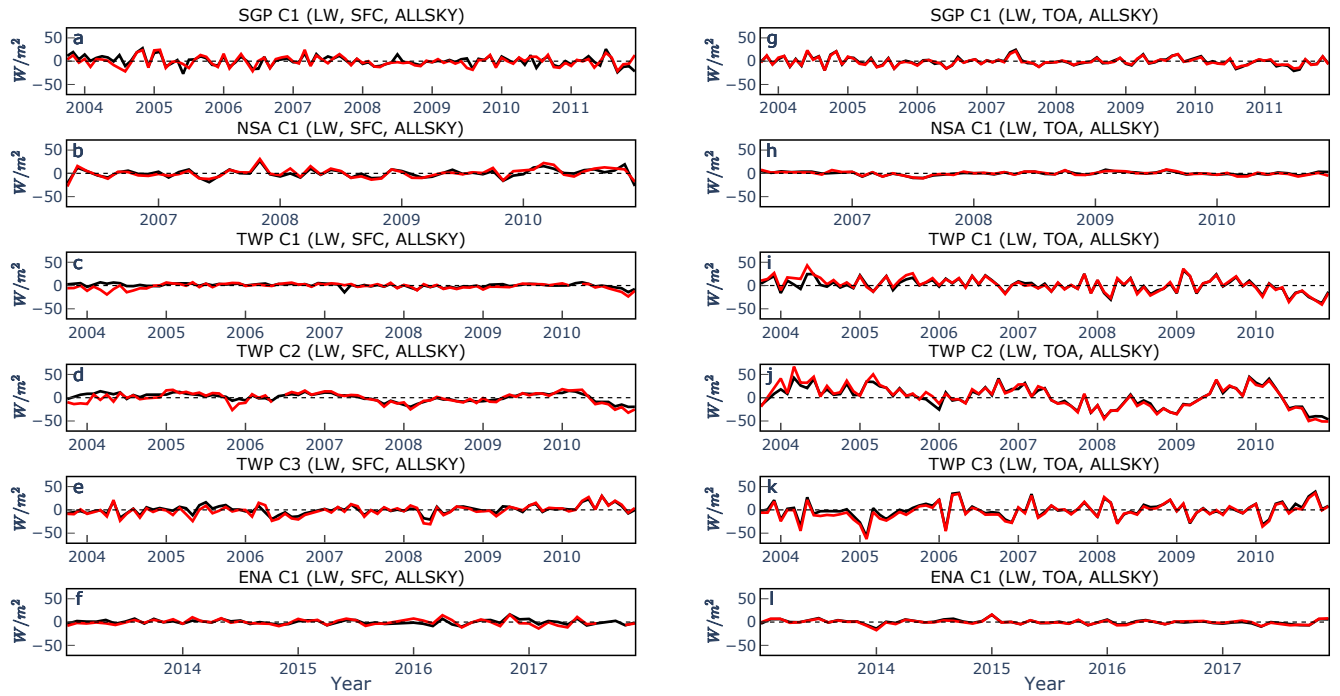
Figure S1. Maximum RMSE of monthly kernel-estimated changes in total-sky SW and LW fluxes calculated with the **ERA5** state variables from the monthly anomalies of **ERA5** total-sky SW and LW fluxes based on periods of different number of months at the six ARM sites. Maximum RMSE of months ranging from 1 to 12 is calculated only using the 12 months of Year 2009. The RMSE of the entire year of 2009 is marked with a dot for each site. The period of 2003/10 – 2010/12 is used to compute maximum RMSE of months ranging from 13 to 88.





— ARM (SFC) or CERES (TOA) flux anomalies — ARM Kernel responses

Figure S2. A comparison of the time series of monthly kernel-estimated changes in total-sky SW fluxes (red) calculated using the **ARM-observed** state variables with monthly anomalies of **ARM-observed** total-sky SW fluxes (black) at SFC (a-f) and of CERES-observed SW fluxes (black) at TOA (g-l) for the six ARM sites.



— ARM (SFC) or CERES (TOA) flux anomalies — ARM Kernel responses

Figure S3. Same as Fig. S2, but for total-sky LW fluxes.

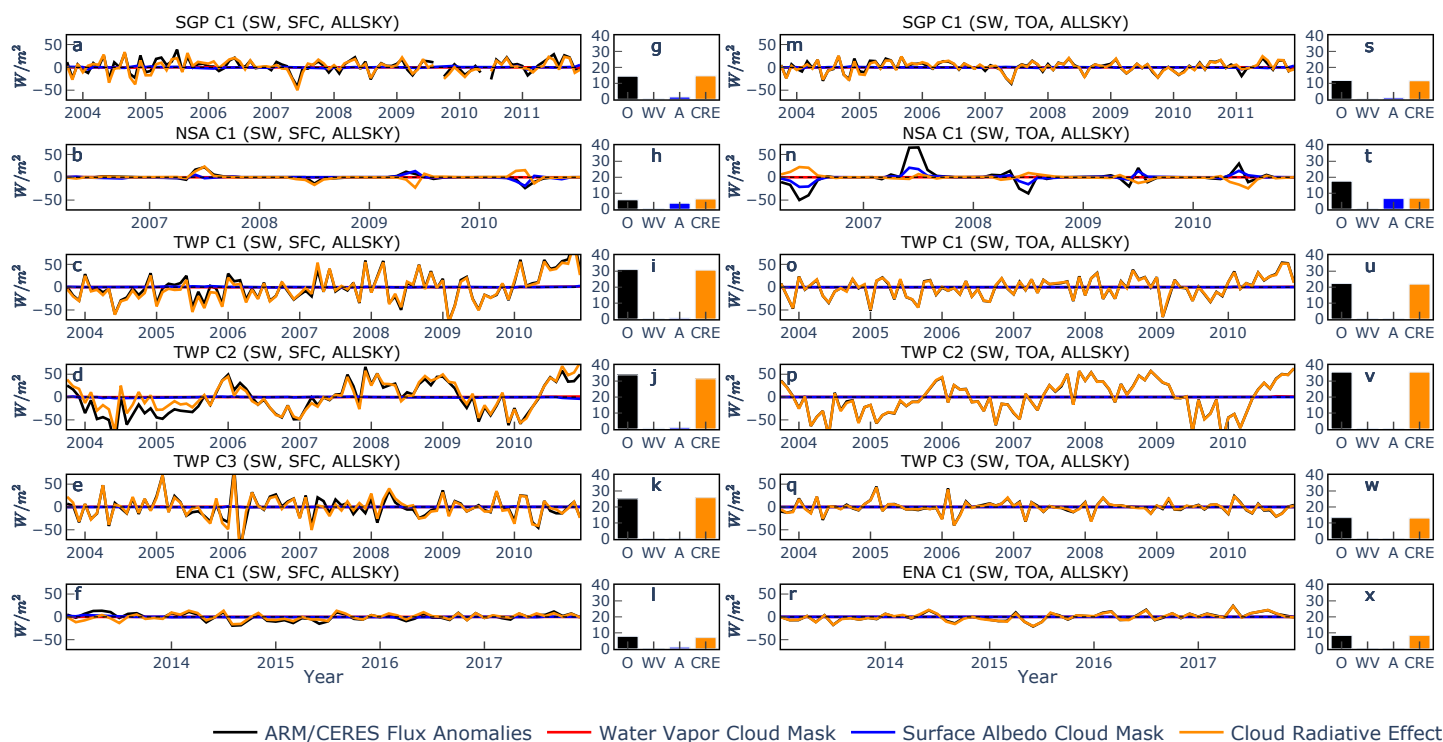


Figure S4. Decomposition of monthly changes in SW dRc in Fig. 5 at SFC (a-f) and TOA (m-r) into changes of water vapor cloud mask (red), surface albedo cloud mask (blue), and cloud radiative effect (dCRE) (orange) for the six ARM sites. These kernel-estimated responses are calculated using **ARM-observed** water vapor and surface albedo. Black line represents monthly anomalies of observed total-sky SW fluxes from ARM (for SFC) and CERES (for TOA). g-l, bar charts of standard deviation of lines in a-f. s-x, bar charts of standard deviation of lines in m-r. Black bar (O) stands for standard deviation of total-sky SW flux anomalies from ARM or CERES, red for SW water vapor cloud mask, blue for surface albedo cloud mask, and orange for dCRE.

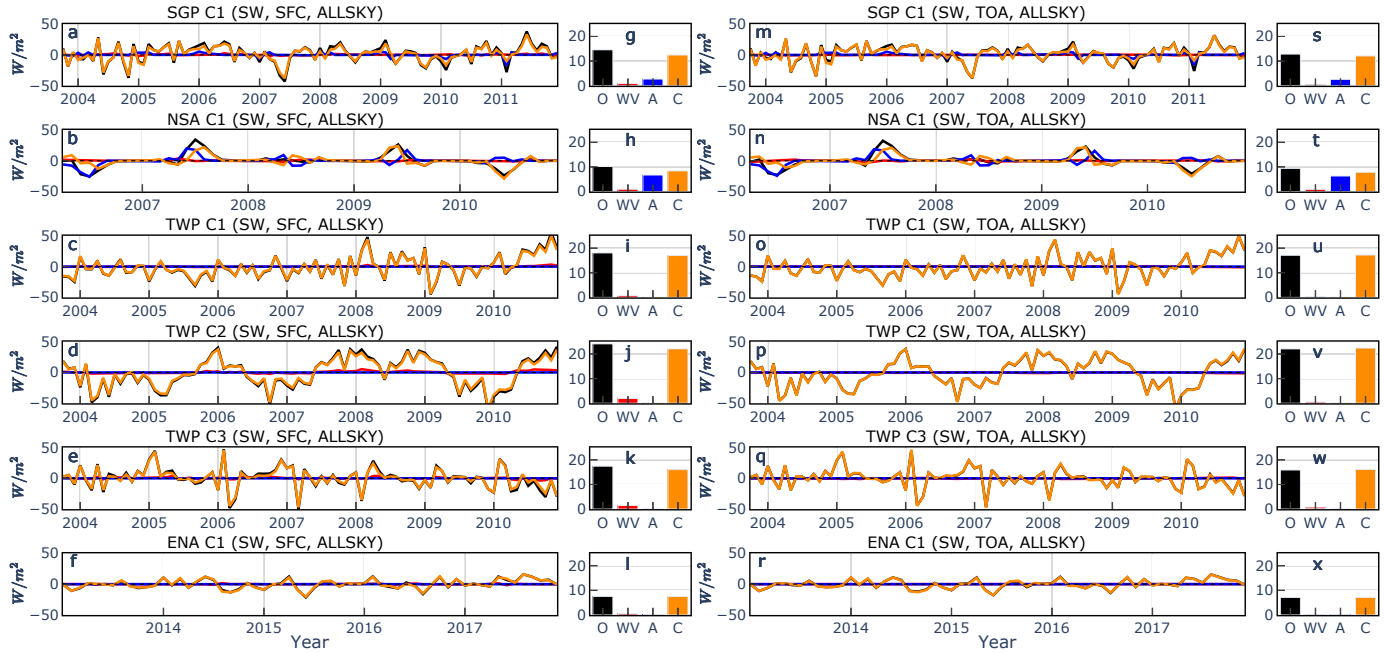


Figure S5. Decomposition of monthly kernel-estimated changes in **ERA5** total-sky SW fluxes at SFC (a-f) and TOA (m-r) into SW water vapor (red), surface albedo (blue), and cloud (orange) kernel-estimated changes for the six ARM sites. These kernel-estimated responses are calculated using **ERA5** water vapor and surface albedo as state variables. Black line represents monthly anomalies of total-sky SW fluxes from ERA5. g-l, bar charts of standard deviation of lines in a-f. s-x, bar charts of standard deviation of lines in m-r. Black bar (O) stands for standard deviation of total-sky SW flux anomalies from ERA5, red for water vapor kernel-estimated changes in SW fluxes, blue for surface albedo kernel-estimated changes, and orange for cloud kernel-estimated changes.

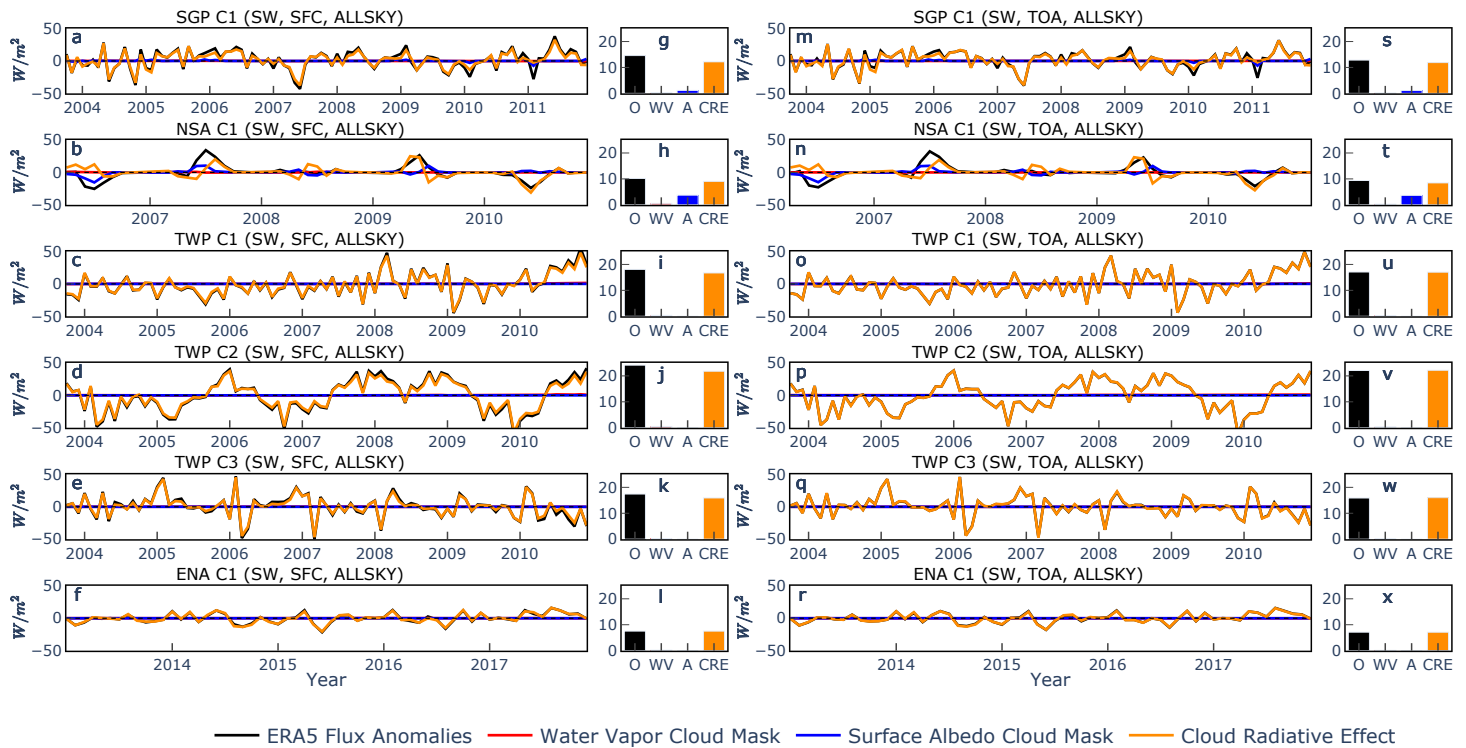
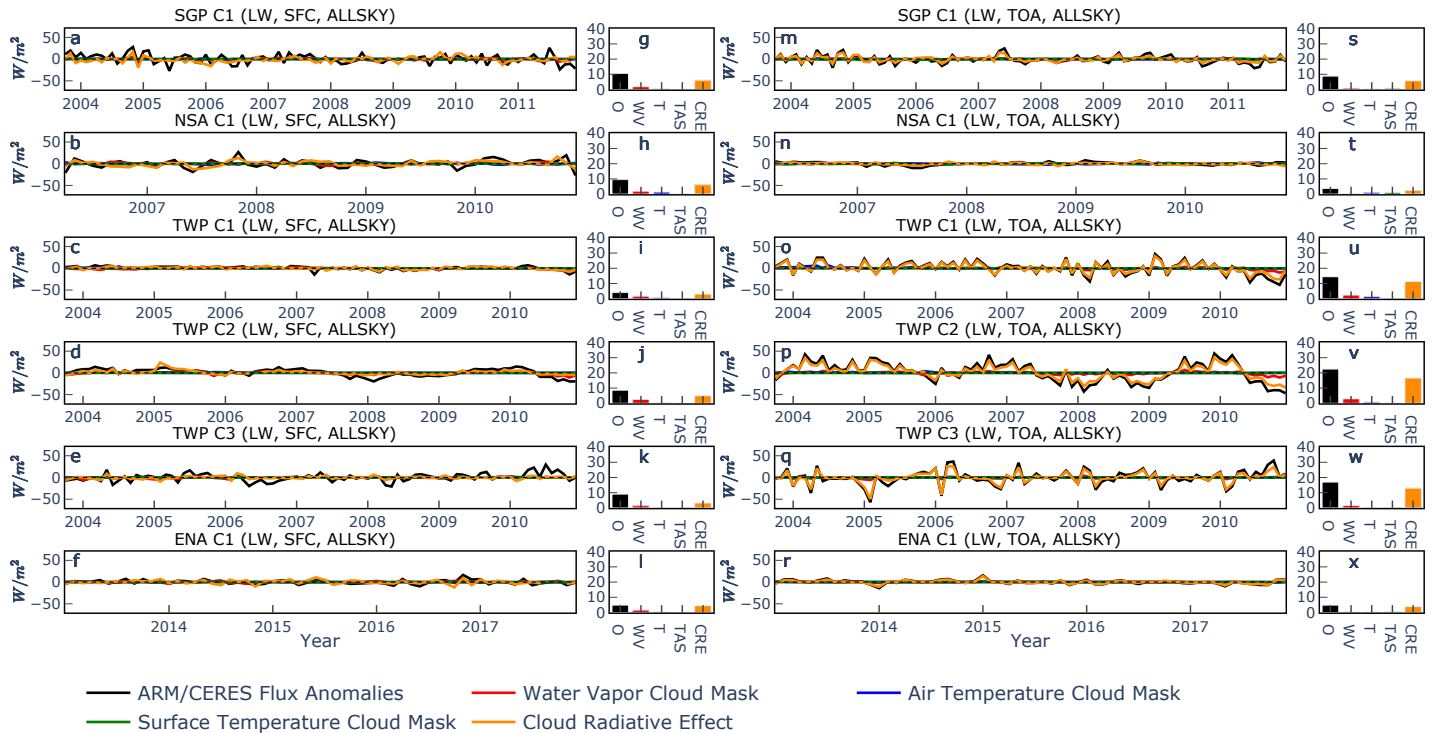


Figure S6. Decomposition of monthly changes in SW dRc in Fig. S5 at SFC (a-f) and TOA (m-r) into changes of SW water vapor cloud mask (red), surface albedo cloud mask (blue), and cloud radiative effect (dCRE) (orange) for the six ARM sites. The kernel-estimated responses are calculated using **ERA5** water vapor and surface albedo as state variables. Black line represents monthly anomalies of total-sky SW fluxes from ERA5. g-l, bar charts of standard deviation of lines in a-f. s-x, bar charts of standard deviation of lines in m-r. Black bar (O) stands for standard deviation of total-sky SW flux anomalies from ERA5, red for water vapor cloud mask, blue for surface albedo cloud mask, and orange for dCRE.



1142 Figure S7. Decomposition of monthly changes in LW dRc in Fig. 6 at SFC (a-f) and TOA  
 1143 (m-r) into changes of LW water vapor cloud mask (red), air temperature cloud mask (blue),  
 1144 surface temperature cloud mask (blue), and cloud radiative effect (dCRE) (orange) for the  
 1145 six ARM sites. These kernel-estimated responses are calculated using **ARM-observed**  
 1146 water vapor and air and surface temperature. Black line represents monthly anomalies of  
 1147 observed total-sky LW fluxes from ARM (for SFC) and CERES (for TOA). g-l, bar charts  
 1148 of standard deviation of lines in a-f. s-x, bar charts of standard deviation of lines in m-r.  
 1149 Black bar (O) stands for standard deviation of total-sky LW flux anomalies from ARM or  
 1150 CERES, red for water vapor cloud mask, blue for air temperature cloud mask, green for  
 1151 surface temperature cloud mask, and orange for dCRE.  
 1152

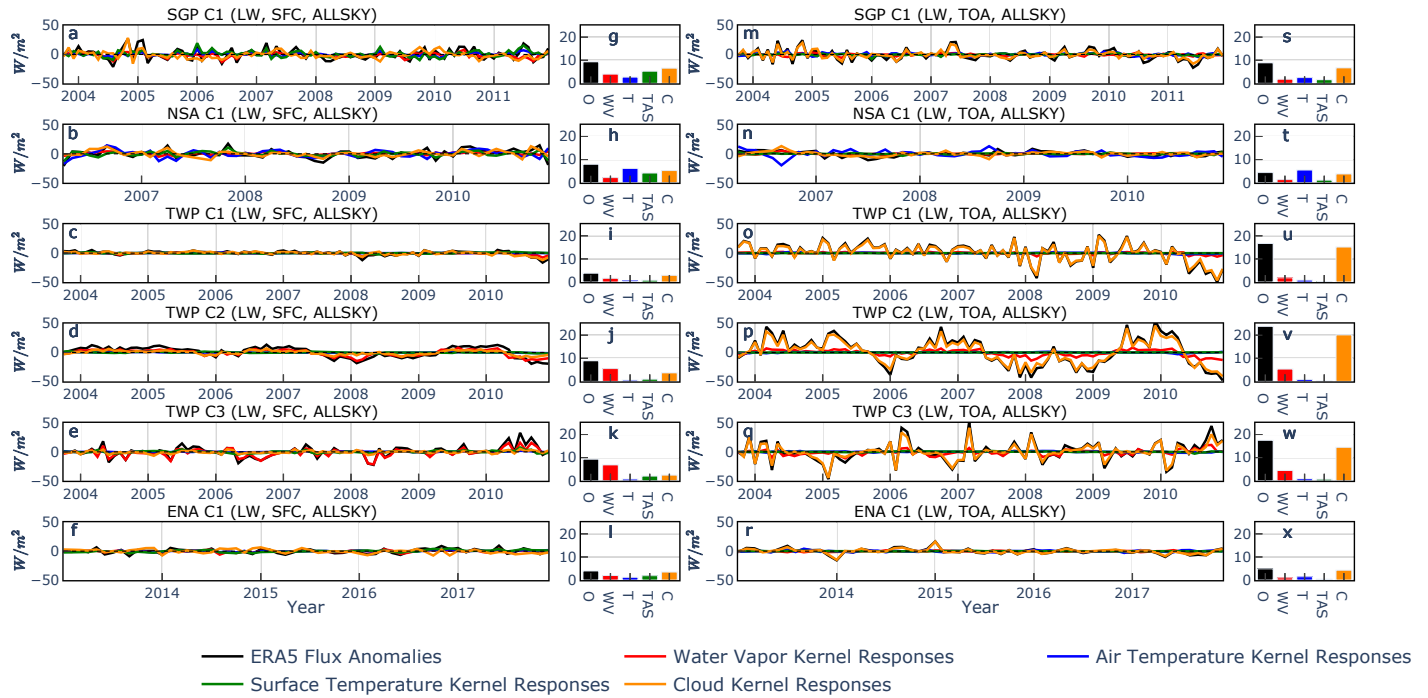


Figure S8. Decomposition of monthly kernel-estimated changes in **ERA5** total-sky LW fluxes at SFC (a-f) and TOA (m-r) into LW water vapor (red), air temperature (blue), surface temperature (green), and cloud (orange) kernel-estimated changes for the six ARM sites. These kernel-estimated responses are calculated using **ERA5** water vapor and air and surface temperature as state variables. Black line represents monthly anomalies of total-sky LW fluxes from ERA5. g-l, bar charts of standard deviation of lines in a-f. s-x, bar charts of standard deviation of lines in m-r. Black bar (O) stands for standard deviation of total-sky LW flux anomalies from ERA5, red for water vapor kernel-estimated changes in LW fluxes, blue for surface albedo kernel-estimated changes, and orange for cloud kernel-estimated changes.

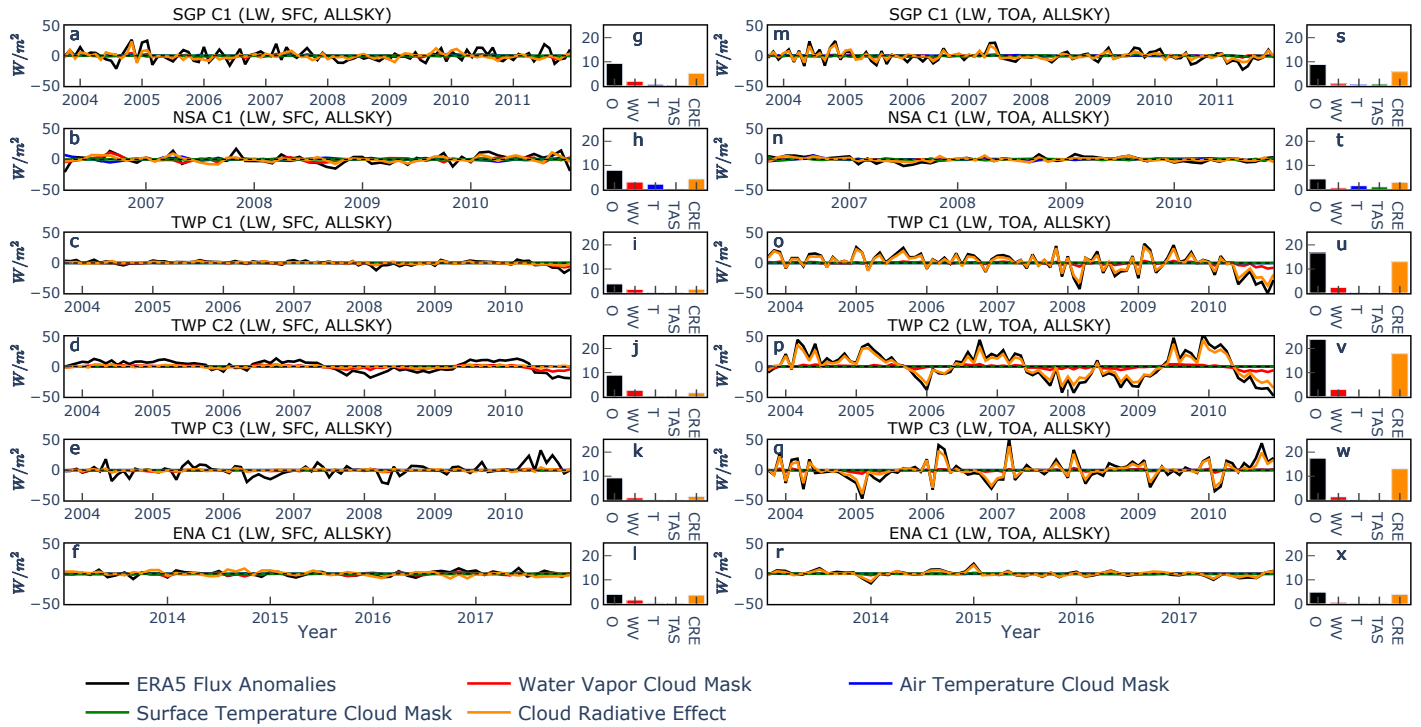


Figure S9. Decomposition of monthly changes in LW dRc in Fig. S8 at SFC (a-f) and TOA (m-r) into changes of LW water vapor cloud mask (red), air temperature cloud mask (blue), surface temperature cloud mask (blue), and cloud radiative effect (dCRE) (orange) for the six ARM sites. These kernel-estimated responses are calculated using ERA5 water vapor and air and surface temperature. Black line represents monthly anomalies of observed total-sky LW fluxes from ERA5. g-l, bar charts of standard deviation of lines in a-f. s-x, bar charts of standard deviation of lines in m-r. Black bar (O) stands for standard deviation of total-sky LW flux anomalies from ERA5, red for water vapor cloud mask, blue for air temperature cloud mask, green for surface temperature cloud mask, and orange for dCRE.